# Zero Thermal Expansion in $ZrMgMo_3O_{12}$: NMR Crystallography Reveals Origins of Thermoelastic Properties

Carl P. Romao,[1] Frédéric A. Perras,[2] Ulrike Werner-Zwanziger,[1] Joey A. Lussier,[3] Kimberly J. Miller,[1] Courtney M. Calahoo,[1] Josef W. Zwanziger,[1,4] Mario Bieringer,[3] Bojan A. Marinkovic,[5] David L. Bryce[2] and Mary Anne White[1,4,*]

[1] Department of Chemistry, Dalhousie University, Halifax B3H 4R2, Nova Scotia, Canada

[2] Department of Chemistry, University of Ottawa, Ottawa K1N 6N5, Ontario, Canada

[3] Department of Chemistry, University of Manitoba, Winnipeg R3T 2N2, Manitoba, Canada

[4] Institute for Research in Materials, Dalhousie University, Nova Scotia B3H 4R2, Halifax, Canada

[5] Departamento de Engenharia Química e de Materiais, Pontifícia Universidade Católica de Rio de Janeiro – PUC-Rio, Rua Marquês de São Vicente 225, Gávea, Rio de Janeiro, RJ, Brasil

[*] Author for correspondence; email: mawhite@dal.ca

**ABSTRACT**

The coefficient of thermal expansion of $ZrMgMo_3O_{12}$ has been measured and was found to be extremely close to zero over a wide temperature range including room temperature ($\alpha_\ell$ = $(1.6 \pm 0.2) \times 10^{-7}$ $K^{-1}$ from 25 °C to 450 °C from XRD). $ZrMgMo_3O_{12}$ belongs to the family of $AMgM_3O_{12}$ materials, for which coefficients of thermal expansion have previously been reported to range from low-positive to low-negative. However, the low thermal expansion property had not previously been explained because atomic position information was not available for any members of this family of materials. We determined the structure of $ZrMgMo_3O_{12}$ by NMR crystallography, using $^{91}Zr$, $^{25}Mg$, $^{95}Mo$, and $^{17}O$ MAS and $^{17}O$ MQMAS NMR in conjunction with XRD and DFT calculations. The resulting structure was of sufficient detail that the observed zero thermal expansion could be explained using quantitative measures of the properties of the coordination polyhedra. We also found that $ZrMgMo_3O_{12}$ shows significant ionic conductivity, a property that is also related to its structure.

## INTRODUCTION

Most materials expand when heated, and the resulting thermal stress can lead to catastrophic material failure. Therefore, there has been considerable recent interest in thermomiotic materials (also known as negative thermal expansion [NTE] materials)[1,2,3,4,5,6] due to their potential to create novel zero thermal expansion materials. There are two primary ways to achieve this goal: by using thermomiotic materials in combination with positive thermal expansion materials,[7,8,9] and by tailoring their structural features chemically in order to produce a material with an intrinsic zero coefficient of thermal expansion (CTE).[10,11,12,13,14,15,16,17,18,19,20] The second route avoids potential problems involving thermal expansion mismatch and can, in theory, lead to zero-thermal-expansion materials that would experience no thermal stress. Here we show that $ZrMgMo_3O_{12}$ exhibits zero thermal expansion over a wide temperature range, and we relate this exceptional property to its structure, as determined by NMR crystallography.

Negative or low thermal expansion in materials composed of corner-linked coordination polyhedra is known to arise from cooperative rotations of the polyhedra generally attributed to librational vibrations of bridging oxygen atoms.[1,2,21] These cooperative rotations lead to shrinkage of the material and therefore have been used to understand NTE in $ZrW_2O_8$ (the most well-studied thermomiotic oxide) *via* the rigid-unit model, in which the internal bond angles of the polyhedra do not change with temperature during the low-frequency vibrations which cause NTE.[1,22]

$ZrMgMo_3O_{12}$ belongs to a group of materials that have the general formula $AMgM_3O_{12}$, where $A$ is a tetravalent cation such as $Zr^{4+}$ or $Hf^{4+}$ and $M$ is $Mo^{6+}$ or $W^{6+}$. These materials typically have low-magnitude CTEs at room temperature.[23,24,25] Their CTEs are chemically tunable by aliovalent substitution of a trivalent $A'$ cation to produce $A'_{2-2x}(AMg)_xM_3O_{12}$ materials.

[17,18] They are also of interest because of the high ionic conductivity reported for $HfMgW_3O_{12}$.[26,27] $AMgM_3O_{12}$ materials display low-magnitude thermal expansion in an orthorhombic space group, which had previously been determined through indexing analysis to be either $Pna2_1$ or *Pnma*.[24,28] However, no atomic-level crystal structures of $AMgM_3O_{12}$ materials have been determined, although an alternating alignment of $Hf^{4+}$ and $Mg^{2+}$ ions along (010) was indicated by high-resolution TEM in $HfMgW_3O_{12}$.[26] The absence of structural information has precluded understanding of the mechanisms of thermal expansion in these materials, especially regarding the origins of low-magnitude thermal expansion.

$AMgM_3O_{12}$ materials are related to the $A_2M_3O_{12}$ family of thermomiotic materials, where *A* is a trivalent cation and *M* is $Mo^{6+}$ or $W^{6+}$. This family has a great deal of chemical flexibility as the *A* site can accommodate atoms ranging in size from $Al^{3+}$ to $Y^{3+}$ and solid solutions of intermediate composition.[19] These materials have CTEs that range from low positive to high negative thermal expansion.[2,19] Their thermal expansion is typically highly anisotropic, with some crystal axes displaying negative thermal expansion while others display positive thermal expansion. The thermal expansion anisotropy can lead to microcracking in sintered polycrystalline bodies.[29]

$A_2M_3O_{12}$ materials display such useful thermal expansion properties when they adopt the orthorhombic *Pbcn* space group. In this arrangement they adopt the $Sc_2W_3O_{12}$ structure,[30] consisting of corner-linked $AO_6$ octahedra and $MO_4$ tetrahedra. The unit cell of the $Sc_2W_3O_{12}$ structure contains 68 atoms; this large unit cell, and the great difficulty of producing single crystals from volatile $MoO_3$ and $WO_3$ precursors,[2] obfuscates structure determination in $A_2M_3O_{12}$ and $AMgM_3O_{12}$ materials. Many $A_2M_3O_{12}$ materials exhibit a displacive phase transformation to a monoclinic $P2_1/a$ phase at temperatures lower than 500 °C and for some of them even far

below room temperature. Monoclinic $P2_1/a$ phases show positive CTEs somewhat higher than the CTEs of traditional ceramics.[2]

Thermal expansivity in $A_2M_3O_{12}$ materials has been shown to correlate negatively with the inherent distortion of the $AO_6$ polyhedron[31,32] defined as the difference between the volume of the real polyhedron and an ideal polyhedron with the same circumscribed sphere radius.[33] For $A_2M_3O_{12}$ materials for which atomic positions at various temperatures have been reported, the inherent distortion correlates with the derivative of distortion with temperature, and it has been suggested that non-rigidity of coordination polyhedra enhances NTE in the $A_2M_3O_{12}$ structure.[31] Therefore, these materials are proposed to have quasi-rigid-unit modes which lead to NTE, similar to those observed in $ZrP_2O_7$.[31,34,35]

Much effort has been expended in recent years towards the goal of solving, or refining, crystallographic structures with the use of solid-state NMR data, sometimes in combination with theoretical modeling and powder diffraction. This approach has come to be known as NMR crystallography.[36,37] Spin diffusion data have been used to determine the crystal packing of organic molecules[38,39,40] and $^1$H chemical shifts have been used either explicitly,[41] or as a crystal structure selection parameter,[42,43] when performing computational crystal structure predictions. Information concerning the connectivity in zeolites[44,45] and aluminophosphates[46,4748] has also been used to solve the crystal structure of framework systems *ab initio*. Chemical shift tensor parameters have additionally been used as refinement parameters for both framework[49,50] and molecular structures.[51]

However, solving, or refining, the crystal structures of inorganic materials using NMR is very challenging as most of the elements involved in such systems are quadrupolar (*i.e.*, have a

spin quantum number, $I \geq 1$), and many also have low resonance frequencies. For such systems, sophisticated correlation experiments are usually out of the question and the accessible observables in favorable situations only include the number of crystallographically distinct sites of a given element, the chemical shifts, and the electric field gradient (EFG) tensor parameters. Fortunately, the EFG tensor can be rapidly, and accurately, computed from PAW DFT[52] calculations and has been used as a constraint for the refinement of the crystal structures of magnesium bromide,[53] sodium aluminoborate,[54] and sodium diphosphates.[55]

$ZrMgMo_3O_{12}$ is an ideal candidate for such a crystal structure refinement approach as the EFG tensors for all of the nuclei ($^{17}O$, $^{25}Mg$, $^{91}Zr$ and $^{95}Mo$) can be determined experimentally via solid-state NMR. Additionally, the number of magnetically distinct sites determined for each element can serve as a constraint when delineating the appropriate space group and can validate a structural model. NMR spectroscopy has been shown to be particularly useful in helping to elucidate the mechanism responsible for NTE in other materials.[56,57,58,59] Furthermore, as we show below, $ZrMgMo_3O_{12}$ exhibits zero thermal expansion over a wide temperature range, and the NMR crystallography approach is able to provide a structure that is sufficiently accurate to delineate the origins of the remarkable CTE.

## EXPERIMENTAL SECTION

To perform a comprehensive characterization of the thermoelastic properties of $ZrMgMo_3O_{12}$ and determine its structure, various experiments were carried out at different temperatures and temperature ranges. A summary of the experiments performed and the temperature ranges of measurement is provided in Table S1 in the Supporting Information.

**Synthesis of $ZrMgMo_3O_{12}$.** $ZrMgMo_3O_{12}$ was synthesized by a solid-state reaction method. In the first step, $ZrO_2$ (Aldrich, 99 %), $Mg_5(CO_3)_4(OH)_2 \cdot 5H_2O$ (Alfa Aesar, 98 %), and $MoO_3$ (Sigma-Aldrich, 99.5 %) were mixed and mechanically activated[2] in a high-energy ball mill for 12 h using stabilized zirconia grinding media and a steel ball mill. The resulting precursor powder was pressed into pellets using a cylindrical die (15 mm diameter) under *ca*. 55 MPa of uniaxial pressure. Reactive sintering of the pellets for 12 h at 700 °C in air formed $ZrMgMo_3O_{12}$, as confirmed by XRD (> 99 % pure). Samples were synthesized using this method for all the reported experiments, except for the $^{17}O$ NMR studies.

**Synthesis of $^{17}O$-enriched sample.** $^{17}O$-enriched $MoO_3$ was synthesized by hydrolysis of $MoCl_5$ as a precursor to $^{17}O$-enriched $ZrMgMo_3O_{12}$. In a dry $N_2$ atmosphere in a glove box, 1.7375 g $MoCl_5$ (Alfa Aesar, 99.6 %) was sealed with a magnetic stir bar in a dry round-bottom flask. The flask was then placed in an ice bath on a magnetic stir plate. Using a syringe, 5 mL of $CCl_4$ was added to dissolve the $MoCl_5$, followed by 0.4958 g enriched $H_2O$ (Aldrich, 40 to 45 atom % $^{17}O$). The reaction was allowed to proceed for 24 h, yielding a green-black solid. The flask was then opened and placed in a sand bath held at 150 °C to evaporate the $CCl_4$; 1.269 g of solid product was subsequently recovered. This solid was presumed to be a mixture of molybdenum oxides, hydroxides, and chlorides,[60] but was not characterizable from diffraction patterns in the PDF-2 database. To determine the yield of $Mo^{17}O_x$ from the reaction of $MoCl_5$ with $H_2{}^{17}O$, a small portion of the product was held at 500 °C for 3 h in an inert atmosphere to remove the hydroxides and chlorides from the solid, giving a black solid which was identified from XRD by Match! phase analysis software as approximately 67 % $MoO_2$ and 33 % $Mo_4O_{11}$. The remaining hydrolysis product was subsequently heated to a temperature of 500 °C for 2 h in air, producing a pale blue-green solid that was confirmed by XRD to be $MoO_3$.

During heating a considerable amount of $MoO_x$ was volatilized, resulting in a yield of 57 % for this step. The volatility of $MoO_3$ at 600 °C has been reported to be low (0.1 % $h^{-1}$)[61] in dry atmosphere, but it is enhanced in the presence of water vapour.[61] The $^{17}O$-enriched $MoO_3$ was then mixed with stoichiometric amounts of $ZrO_2$ (Aldrich, 99 %) and $C_4H_2Mg_5O_{14}•5H_2O$ (Alfa Aesar, 98 %) and ball-milled for 6 h in a planetary ball mill with polyurethane grinding jars and stabilized zirconia grinding media. Following milling, the precursor powder was pressed into a pellet and calcined in air at 471 °C for 6 h to remove water, $CO_2$, and any polyurethane, followed by reactive sintering in air at 690 °C for 12 h. The monophasic nature of the resulting $ZrMgMo_3O_{12}$ was confirmed by XRD (> 99% purity). The $^{17}O$-enriched $ZrMgMo_3O_{12}$ was used only for the $^{17}O$ NMR experiments.

**X-Ray Powder Diffraction.** High-temperature X-ray powder diffraction data were collected on a PANalytical X'Pert Pro Bragg-Brentano diffractometer (PANalytical B.V., Almelo, the Netherlands) equipped with a Cu anode ($\lambda(Cu\text{-}K\alpha_1)$ = 1.540598 Å and $\lambda(Cu\text{-}K\alpha_2)$ = 1.544426 Å). The diffractometer used a 1° divergence and a 0.04 rad soller slit assembly for the primary beam and a Ni filter and 0.04 rad soller slits for the diffracted beam. Using an X'Celerator detector (128 microstrips covering 2.122°) each data set was collected for 45 minutes covering the angular range 2θ from 10° to 65° with 0.0167° step size and 100 s/step collection time. The sample was mounted as an acetone slurry directly on the 10 mm platinum resistive strip heater within a self-masking HTK2000 furnace (Anton Paar GmbH). The temperature of the furnace is reliable within 5 K between room temperature and 1200 °C. Variable temperature powder X-ray diffractograms were collected at 25 K increments from 25 °C to 650 °C and then at 25 K steps during cooling to 25 °C. Room-temperature powder X-ray diffraction data were collected on the same PANalytical powder diffractometer equipped with a spinning sample stage (1 Hz) using a

zero-background sample holder, Si(510), and a 10 mm mask. The data were collected with 0.0084° steps covering $10° \leq 2\theta \leq 90°$ with 200 s per step counting time. This diffractogram was used for a Le Bail fit, as well as a preliminary Rietveld fit (see below). The diffractometer line profiles and peak positions were confirmed with $LaB_6$ SRM 660a NIST and Si SRM 640b NIST standards, respectively. To determine the unit cell volume as a function of temperature, X-ray diffractograms were analyzed by the Le Bail method ($Pna2_1$ space group) using FullProf.2k (version 5.30).[62] Each refinement was carried out with 18 parameters including the unit cell parameters *a*, *b* and *c*, the sample displacement parameter, three peak shape parameters for the pseudo-Voigt profile and 11 linearly interpolated background points. Two diffraction peaks originating from the Pt heater (38.6° to 41.0° and 45.0° to 47.0°) were excluded from the refinements. Data at angles below 17.5° were excluded because of excessive peak asymmetry. The zero-point and asymmetry parameters were fixed during the refinements after those were determined from the room-temperature powder X-ray diffraction data collected on a spinning zero-background holder with no sample displacement. All refinements converged with final $\chi^2$ (goodness of fit) values between 4 and 8. The refinements were carried out on the data acquired from room temperature to 650 °C for both heating and cooling, for determination of intrinsic thermal expansion.

**Dilatometry.** The bulk CTE of $ZrMgMo_3O_{12}$ was measured using a NETZSCH 402 C alumina push-rod dilatometer. The measurements were performed from room temperature to 700 °C at a heating rate of 10 K $min^{-1}$, and at a natural cooling rate of approximately 5 K $min^{-1}$. The instrument was calibrated using a fused quartz standard matched in length to the sample to within 5 %. The standard uncertainty of the instrument in $\Delta\ell/\ell_0$ was ± 1%.[17,63]

**Thermal Analysis.** Differential scanning calorimetry (DSC) was used to delineate any

phase transitions in $ZrMgMo_3O_{12}$ with a 20.43 mg sample in an aluminum pan using a TA Instruments Q200 series DSC equipped with a liquid $N_2$ cooling head. The temperature range studied was −175 °C to 35 °C with a temperature ramp rate of 5 K $min^{-1}$. The instrument was calibrated using a 5.12 mg sample of indium in an aluminum pan. Measurements were performed under He purge gas.

TGA was performed on a 21.74 mg sample of $ZrMgMo_3O_{12}$ to determine whether the material had taken up water from the atmosphere, and to determine its decomposition temperature. The sample was heated in a fused $SiO_2$ crucible in a NETSZCH TG 209 F3 instrument from room temperature to 900 °C in Ar atmosphere.

**$^{25}$Mg NMR.** The $^{25}$Mg MAS NMR spectrum at 9.4 T ($\nu_L(^{25}Mg)$ = 24.5 MHz ) was acquired using a Hahn echo sequence preceded by a double-frequency (DFS) pulse sweeping from 300 to 20 MHz in 5 ms for signal enhancement.[64,65] The sample was spun at 5 kHz using a 7 mm low-γ MAS probe. The central transition (CT) selective 90° and 180° pulses lasted 12 and 24 μs respectively, and the echo delay was 200 μs. In total 14504 scans were acquired with a 4 s recycle delay. The chemical shifts were referenced to a saturated $MgCl_2$ solution in water. The $^{25}$Mg MAS NMR spectrum at 21.1 T ($\nu_L(^{25}Mg)$ = 55.1 MHz ) was acquired using a simple Bloch decay sequence with a 3 μs CT-selective excitation pulse. The sample was spun at 10 kHz using a 4 mm low-$\gamma$ MAS probe. In total 712 scans were accumulated with a 2 s recycle delay.

**$^{91}$Zr NMR**. A static $^{91}$Zr NMR spectrum was acquired at 9.4 T ($\nu_L(^{91}Zr)$ = 37.2 MHz) using a Hahn echo sequence preceded by a DFS pulse sweeping from 1 MHz to 100 kHz in 5 ms. The data were acquired with a 7 mm solenoid probe using 35992 scans and a 0.5 s recycle delay. A 5 μs CT-selective 90° pulse was used along with a 50 μs echo delay. The chemical shifts were referenced to a solution of $Cp_2ZrCl_2$ in dichloromethane. A static $^{91}$Zr NMR spectrum was

acquired at 21.1 T ($\nu_L(^{91}Zr)$ = 83.7 MHz ) using a Hahn echo sequence preceded by a DFS pulse sweeping from 1 MHz to 50 kHz in 2 ms. A 3 μs CT-selective 90° pulse was used along with a 30 μs echo delay. The data were acquired with a 4 mm MAS probe using 6250 scans and a 1 s recycle delay. An MAS NMR spectrum was also acquired at 21.1 T spinning at 10 kHz. The same experimental parameters were used; however, the echo delay was increased to 100 μs for rotor synchronization and a total of 2560 scans were accumulated.

**$^{95}$Mo NMR.** The $^{95}$Mo MAS NMR spectrum at 9.4 T ($\nu_L(^{95}Mo)$ = 26.1 MHz) was acquired using a Hahn echo sequence preceded by DFS pulse sweeping from 800 to 50 kHz in 5 ms for signal enhancement. The sample was spun at 5 kHz using a 7 mm low-γ MAS probe. The CT-selective 90° and 180° pulses lasted 8 μs and 16 μs respectively, and the echo delay was 200 μs. In total, 18968 scans were acquired with an 8 s recycle delay. The chemical shifts were referenced to a 2 molal solution of $Na_2MoO_4$ in water. A $^{95}$Mo MAS NMR spectrum was also acquired at 11.7 T ($\nu_L(^{95}Mo)$ = 32.6 MHz) using a Hahn echo sequence preceded by a DFS pulse sweeping from 1 MHz to 80 kHz in 5 ms for signal enhancement. The sample was spun at 10 kHz using a 4 mm low-$\gamma$ MAS probe. The CT-selective 90° and 180° pulses lasted 6.67 μs and 13.34 μs respectively, and the echo delay was 100 μs. In total, 11528 scans were acquired with a 10 s recycle delay. A $^{95}$Mo MAS NMR spectrum was also acquired at 21.1 T ($\nu_L(^{95}Mo)$ = 58.6 MHz) using a Bloch decay sequence. The sample was spun at 10 kHz using a 4 mm low-$\gamma$ MAS probe. The CT-selective excitation pulse lasted 3 μs. In total 128 scans were acquired with a 5 s recycle delay. An MQMAS NMR spectrum[66] was also acquired using the three-pulse sequence with a z-filter.[67] The excitation, conversion, and detection pulses lasted 8 μs, 3 μs, and 20 μs, respectively. A total of 45 $t_1$ increments of 100 μs were acquired with 240 scans each.

**$^{17}$O NMR.** $^{17}$O MAS NMR spectra were acquired at 9.4 T, 16.5 T, and 21.1 T magnetic field strengths ($^{17}$O NMR Larmor frequencies of 54 MHz, 95 MHz and 122 MHz, respectively). The samples were spun up to 13.5 kHz using 4 mm MAS probes (9.4 T and 16.5 T instruments) and up to 26 kHz at 21.1 T using a 2.5 mm MAS probe. Short excitation pulses (0.54 μs at 53 kHz rf power [9.4T], 0.69 μs at 41 kHz rf power [16.4 T], and 0.5 μs at 83 kHz rf power [21.1 T], respectively) were applied and between 1200 and 148000 scans were collected (depending on instrument and rotor sizes) at recycle delays of 0.5 to 1 s. The spectra showed severe baseline rolls due to pulse ring down, which were removed either by linear back projection and baseline corrections or by left-shifting the FID to the earliest rotational echo. The chemical shift scales were referenced externally against water at 0 ppm. An $^{17}$O 3QMAS NMR spectrum was acquired with 10 kHz sample spinning at 16.4 T. The transmitter was set to 488 ppm and the $F_1$ sweep width to 10 kHz. 15 $t_1$ slices each with 288 scans were acquired using 20 s recycle delays. The $F_1$ axes were scaled and referenced according to the $C_z$ convention of Millot et al.[68] and inverted due to the echo acquisition.

**NMR Crystallography.** Static $^{91}$Zr NMR spectra were fit using the QUEST program,[69] whereas DMfit[70] was used to fit the MAS NMR spectra. The two-dimensional-one-pulse procedure, used to sum the spinning sidebands, was implemented using the DMfit program.[71] All PAW and GIPAW DFT calculations were performed using the CASTEP program (ver. 3.2 or 4.1).[52,72,73,74] The GGA functional of Perdew, Burke, and Ernzerhof (PBE)[75] was used for all the DFT calculations. A 3×3×2 *k*-point grid was used along with a 610 eV kinetic energy cut-off. On-the-fly generated ultrasoft pseudopotentials were used for all atoms. The accuracy of the PAW DFT predicted EFG tensor components was determined by performing calculations on model systems with known crystal structures and EFG tensor parameters (see Figure S1 in the

Supporting Information). This approach makes it possible to also determine the factors by which the PAW DFT calculations systematically over- or under-estimate the EFG tensor components for each element. This over- or under-estimation of the EFG tensor components can arise from incompleteness of the PAW bases and also from the exchange and correlation functional model used.[54] It is important to estimate these factors when refining crystal structures using experimental EFG tensor parameters and PAW DFT calculations, as otherwise the polyhedral distortions would be under- or over-estimated. Our calibration curves for $^{17}O$, $^{25}Mg$, $^{91}Zr$, and $^{95}Mo$ showed that the calculated EFG tensor parameters are scaled by $1.029 \pm 0.007$[†] for $^{17}O$, $1.14 \pm 0.04$ for $^{25}Mg$, $0.93 \pm 0.04$ for $^{91}Zr$, and $1.11 \pm 0.02$ for $^{95}Mo$, when compared to experiment. The small deviations on the calibration factors, each of the order of a few percent at most, indicate the precision of this method. Because the compounds used to assess the calculations include many examples of bonding environments similar to those expected in $ZrMgMo_3O_{12}$, we are therefore confident in using the calculated EFG tensor parameters, in addition to the empirical scaling factors, to accurately refine the crystal structure. The calibration curves are shown in Figure S1 in the Supporting Information

The geometry optimization of the crystal structure was performed with fixed unit cell dimensions determined from the Rietveld analysis (see below). The NMR/DFT-refinement of the crystal structure was subsequently performed using a steepest descent least-squares minimization of the $\chi^2$ parameter, *vide infra*, as previously described.[54] All DFT calculations in the refinement process calculated only the EFG due to its significantly lower computational cost, when compared to the magnetic shielding. Convergence was achieved after three iteration steps, which corresponds to a total of 174 PAW DFT calculations for the refinement of the crystal structure.

[†] Uncertainties correspond to the standard error of the fit.

Relativistic DFT calculations were performed using the Amsterdam Density Functional (ADF) program.[76] Two-component (scalar and spin-orbit) relativistic effects were included using the zeroth-order regular approximation (ZORA),[77] as implemented in ADF. Calculations with and without relativistic effects were performed on *A*-O-Mo (*A* being either Mg or Zr) clusters; the difference in chemical shifts between the two is the spin-orbit ZORA relativistic shift. Calculations on larger clusters generally had SCF convergence issues; this is a known problem for transition metal oxide systems. Calculations were performed using the PBE GGA functional and the ZORA/TZ2P Slater basis set.

**Raman Spectroscopy.** The Raman spectrum of $ZrMgMo_3O_{12}$ was collected at room temperature using a Nicolet NXR 9650 FT-Raman spectrometer with a 1064 nm excitation laser, with spectral resolution of 1 $cm^{-1}$.

**Mechanical Properties.** The mechanical properties of $ZrMgMo_3O_{12}$ were determined by measurement of the transverse and longitudinal velocities of sound at room temperature. A Panametrics Ultrasonic Thickness Gauge was used with Panametrics shear-wave couplant and glycerol (longitudinal-wave couplant) to measure the velocities of sound in three polycrystalline samples (average height 2.8 mm, average diameter 12.3 mm) of $ZrMgMo_3O_{12}$ (density 84 % of theoretical on average). The measured velocities of sound were corrected for porosity as follows:[78]

$$v = v_0(1 - p), \qquad (1)$$

where $v$ is the measured velocity, $v_0$ is the corrected, fully densified velocity, and $p$ is the pore fraction. This correction assumes spherical crystallite morphology which introduces only a small error for pore fractions below about 25 %,[78,79,80] as here.

**Ionic Conductivity.** The electrical impedance of $ZrMgMo_3O_{12}$ was determined using a Solartron SI 1260 Impedance/Gain Phase analyser to assess ionic conductivity. AC impedance of a sintered pellet (12.67 mm diameter, 1.75 mm high) was measured using Pyroduct 597-A electrodes over a temperature range from 340 °C to 520 °C in air (the impedance below 340 °C was too high to perform a reliable measurement). The AC impedance was measured while decreasing the frequency from 3 MHz to 100 Hz, with an amplitude of three different values, 50 mV, 75 mV and 100 mV, to check that the response was linear. The instrumental setup was validated by measuring the ionic conductivity of $Sc_2W_3O_{12}$ in comparison with a literature value (Figure S2 in the Supporting Information).

## RESULTS AND DISCUSSION

**Phase Stability**. DSC of $ZrMgMo_3O_{12}$ showed a solid-solid phase transition at −126 °C on heating and an enthalpy change, $\Delta H$, of 195 J $mol^{-1}$ (Figure S3 in the Supporting Information). Based on the phase transition in $HfMgMo_3O_{12}$ at −98 °C,[81] and solid-solid transitions in many $A_2M_3O_{12}$ materials,[2] $ZrMgMo_3O_{12}$ likely is in a monoclinic $P2_1/a$ phase (with positive thermal expansion; see below) below −126 °C. To determine the upper temperature limit of phase stability, TGA was performed (Figure S4 in the Supporting Information), showing decomposition beginning at *ca*. 750 °C. This information indicates a broad temperature range of stability for the orthorhombic phase of $ZrMgMo_3O_{12}$ (−126 °C to 700 °C).

**Thermal Expansion.** A dilatometric curve for $ZrMgMo_3O_{12}$ on cooling is shown in Figure 1.[‡] The bulk CTE of polycrystalline $ZrMgMo_3O_{12}$ is remarkably small, with an average

[‡] Often, the first heating curve is less representative of the CTE than the cooling curve or subsequent heating curves,[63] as the first heating curve is influenced the most by microcrack healing in the sample and desorption of surface water on the alumina pushrod. These effects are especially prominent here (see Figures S5, S6, and S7 for

value of $\alpha_\ell = (-3 \pm 1)^{\S} \times 10^{-7}\ K^{-1}$ from 23 °C to 500 °C based on seven runs on three samples. From 500 °C to 700 °C the bulk CTE is dominated by extrinsic, microstructural effects (microcrack healing on heating and microcrack formation on cooling).[29]

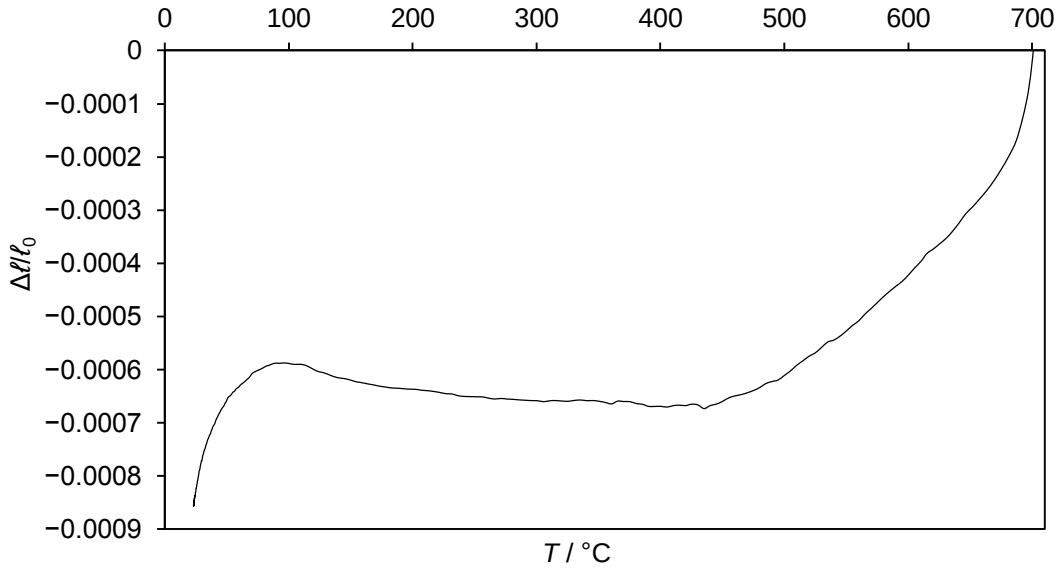


Figure 1: A dilatometric cooling curve for $ZrMgMo_3O_{12}$, starting at 700 °C, showing the change in length with respect to the original length as a function of temperature. The CTE as determined *via* linear regression from 23 °C to 500 °C for this run is $\alpha_\ell = 4.1 \times 10^{-7}\ K^{-1}$.

The inset in Figure 2 shows the powder X-ray diffraction contour plot for $ZrMgMo_3O_{12}$ during heating in air from 25 °C to 650 °C in 25 K increments. Heating beyond 700 °C results in sample decomposition (see TGA results above). The opposite shifts of the (220) and (004) peaks shown in the contour plot indicate anisotropic thermal expansion of the $Pna2_1$ structure (see below regarding the space group). The *a*- and *b*-axes undergo contraction whereas the *c*-axis expands during heating. Furthermore the intrinsic thermal expansion is fully reversible for heating and cooling and no phase transition was observed from room temperature up to 650 °C.

several heating and cooling curves)**Error! Bookmark not defined.** because of the low intrinsic thermal expansivity of $ZrMgMo_3O_{12}$.

§ Uncertainty reported at the 95% confidence level.

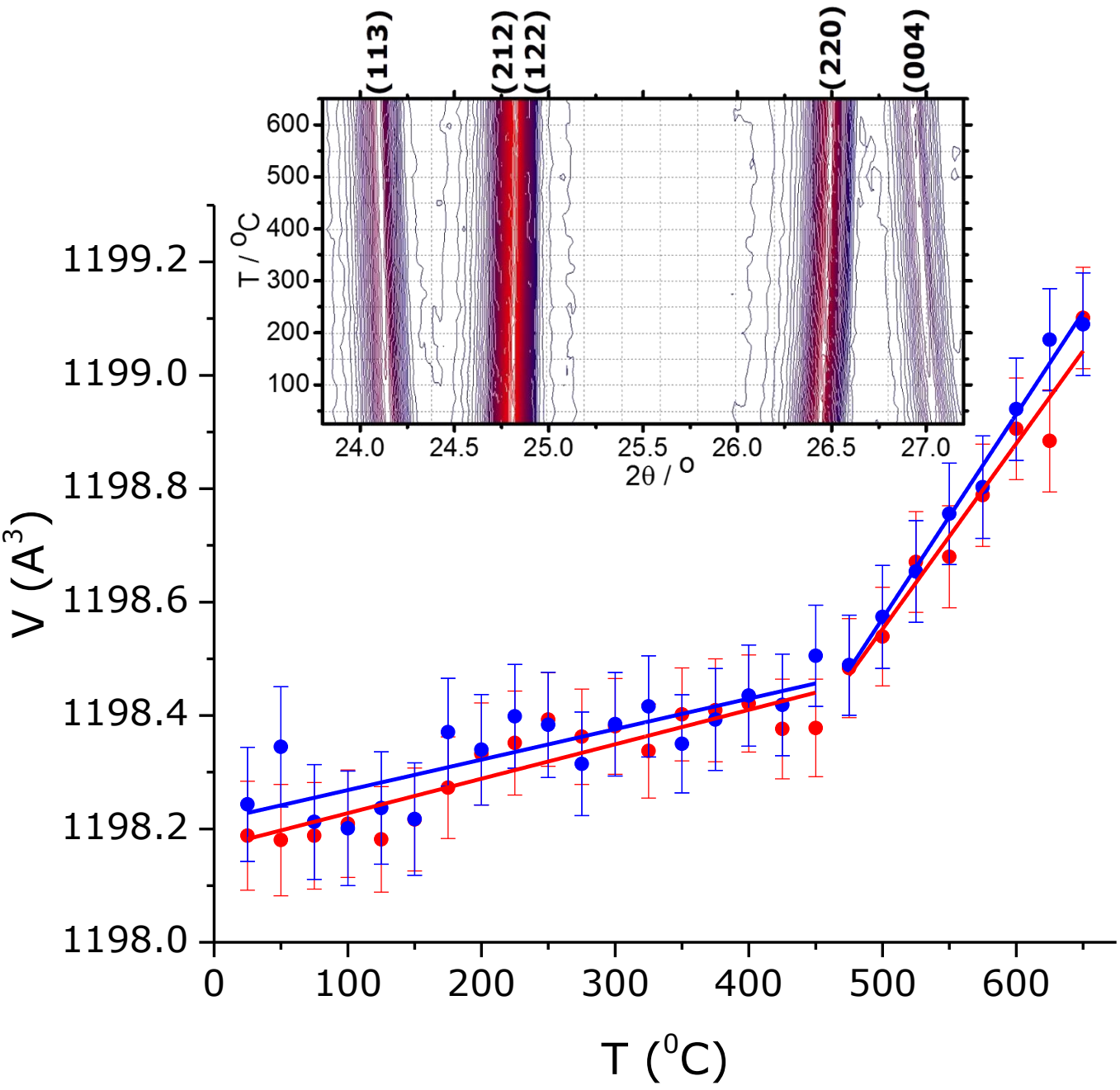


Figure 2: Unit cell volume evolution as a function of temperature as determined by *in-situ* powder X-ray diffraction. The red symbols and lines indicate heating data and linear fits, and the blue symbols and lines indicate cooling data and linear fits. Inset: Representative angular range of the contour plot of the variable temperature powder X-ray diffraction data during heating. Intensities are indicated as contour lines with 50 equal increments between the lowest intensity (blue) and the highest intensity (red). The Miller indices at the top of the inset refer to space group $Pna2_1$.

The temperature-dependent unit cell dimensions were obtained from Le Bail fits; Figure S8 (see Supporting Information) illustrates the fitting quality for the X-ray powder diffraction data collected at 100 °C during cooling. The unit cell volume evolution with temperature for $ZrMgMo_3O_{12}$ for two temperature ranges is shown in Figure 2. $ZrMgMo_3O_{12}$ exhibits a coefficient of intrinsic thermal expansion which is very close to zero between 25 °C and 450 °C during heating ($\alpha_\ell = (1.7 \pm 0.2)^{**} \times 10^{-7}$ K$^{-1}$) and cooling ($\alpha_\ell = (1.5 \pm 0.3) \times 10^{-7}$ K$^{-1}$). By comparison, the CTEs of traditional oxide ceramics are typically 1.5 to 2 orders of magnitude larger than that of $ZrMgMo_3O_{12}$ in this temperature range.[82,83] The magnitude of the CTE of $ZrMgMo_3O_{12}$ is lower across this temperature range than that of many commonly used zero thermal expansion materials such as fused quartz and Invar; it is also lower than that of several zero thermal expansion materials which have recently been reported in the literature.[10,14,15,16,17,18,19,84] Above 450 °C the linear thermal expansion coefficient increases by almost an order of magnitude with values of $\alpha_\ell = (9 \pm 3) \times 10^{-7}$ K$^{-1}$ and $\alpha_\ell = (10 \pm 3) \times 10^{-7}$ K$^{-1}$ during heating and cooling, respectively. The CTE in this temperature range is still quite low by comparison to conventional materials, however.[82,83] The CTE for $ZrMgMo_3O_{12}$ reported herein is considerably closer to zero than was reported by Song *et al.*,[25] and our results are corroborated by the CTE as measured by variable-temperature X-ray diffraction over a much larger set of temperature points (Figure 2), and by dilatometric (Figure S7 in the Supporting Information) and variable-temperature X-ray diffraction (Figure S10 in the Supporting Information) results on a second sample of $ZrMgMo_3O_{12}$ made in a separate synthesis.

Axial CTEs measured on heating are presented in the Supporting Information (Figure S9). Because the CTE of $ZrMgMo_3O_{12}$ is anisotropic, bulk samples could experience thermal

** Uncertainties reported at the 95% confidence level.

stress and microcracking upon heating and cooling.[29,79] However, thermal cycling results (Figures S6 and S7 in the Supporting Information) indicate reduced microcracking effects after the first heating. An important measure of an orthotropic material's propensity for thermal stress is the CTE anisotropy, quantified as $\Delta\alpha_{max}$ (the maximum difference between two axial CTEs). For $ZrMgMo_3O_{12}$ between 25 °C and 450 °C, $\Delta\alpha_{max} = 12 \times 10^{-6}$ $K^{-1}$, a value slightly higher than reported for orthorhombic $In(HfMg)_{0.5}Mo_3O_{12}$, $In_2Mo_3O_{12}$, and $HfMgMo_3O_{12}$;[17] $\Delta\alpha_{max}$ for $ZrMgMo_3O_{12}$ decreases to $8.3 \times 10^{-6}$ $K^{-1}$ over the temperature range 450 °C to 650 °C.

The intrinsic (X-ray derived) thermal expansion coefficients agree qualitatively with the dilatometry results. Both data sets show only very small volume changes from room temperature up to approximately 450 °C and larger expansion at higher temperatures. Notably the dilatometric data indicate a very small negative expansion coefficient up to 450 °C, whereas the intrinsic expansion coefficient is also small but positive. The difference suggests that microstructural effects influence the bulk CTE.

**Mechanical Properties.** Mechanical properties of thermomiotic and near-zero CTE materials are very important in determining their suitability for potential applications, whether they are to be used in bulk form or incorporated in a composite, because they influence the thermal stresses experienced and the degree to which positive thermal expansion can be counteracted.[2,79,80] The transverse and longitudinal velocities of sound of $ZrMgMo_3O_{12}$, corrected to zero porosity, were determined here as $v_t = 2624 \pm 63$ m $s^{-1}$ and $v_l = 4314 \pm 58$ m $s^{-1}$ (uncertainties based on three samples), which correspond to a bulk modulus of 31 ± 3 GPa and a shear modulus of 22 ± 1 GPa, both quite low in comparison to conventional oxide ceramics. Similarly low bulk moduli have been previously reported for several other thermomiotic materials.[2]

**Structure Determination by NMR Crystallography.** The above findings of zero thermal expansion in $ZrMgMo_3O_{12}$ can only be fully understood with detailed knowledge of its structure. However, it was not possible to grow single crystals of $ZrMgMo_3O_{12}$. Furthermore, although the powder diffraction approach can, in principle, resolve unknown crystal structures *ab initio*, powder diffraction experiments using synchrotron x-ray[24] and neutron[28] sources were unable to delineate the crystal structures, or even the space groups, of the related phases $HfMgMo_3O_{12}$ and $HfMgW_3O_{12}$. Therefore, we have taken an alternate structure-determination approach.

To begin the process of structure determination, the free objects in crystallography program (FOX)[85] was used to solve a structural model for $ZrMgMo_3O_{12}$ using standard PXRD data acquired at room temperature ($10° \leq 2\theta \leq 90°$, see Figure S12 in the Supporting Information). FOX is a freely-available Monte Carlo-type *ab initio* crystal structure solution program that uses powder or single-crystal diffraction intensity data to determine the fractional positions of input atoms (typically determined from the empirical formula) within a previously determined unit cell. Three molybdate polyhedra as well as single magnesium and zirconium ions were included in the structure solution. It was not possible to reach convergence using the *Pnma* space group and thus the $Pna2_1$ space group (a subgroup of *Pnma*) was trialed. The latter corresponds to the approximate symmetry that was suggested by density functional theory (DFT) and scanning transmission electron microscopy studies for $HfMgW_3O_{12}$.[26] The structure solved using the $Pna2_1$ space group was consistently reproduced using a series of random starting structures, see Figure S12 (a), providing evidence of its reliability. Using the Rigaku PDXL software, a Rietveld refinement of a FOX-determined structural model was performed. This refinement improved the agreement of the crystal structure with the PXRD pattern (Figure S12

(b)), and made it more reasonable chemically; however many of the bond lengths and angles were still unrealistic. For example, some Zr-O bond lengths were as long as 3 Å and some O-Mo-O angles were as large as 157°, indicating the need for further refinement using DFT and NMR. The Rietveld refinement did, however, allow accurate unit cell dimension determination for $ZrMgMo_3O_{12}$ ($a$ = 9.5737(2) Å, $b$ = 9.4900(2) Å, $c$ = 13.1739(3) Å), in excellent agreement with those from the Le Bail refinement ($a$ = 9.576(2) Å, $b$ = 9.489(2) Å, $c$ = 13.186(4) Å). Then the Rietveld-refined crystal structure was optimized using PAW DFT to obtain a structural model with reasonable bond lengths and angles prior to refinement based on NMR parameters. The connectivity of the coordination polyhedra in this structure is analogous to that in the structure of $Sc_2W_3O_{12}$[30] and features ordering of the Mg and Zr cations as previously reported for $HfMgW_3O_{12}$,[26] suggesting that $ZrMgMo_3O_{12}$ could also have high ionic conductivity.

We acquired a series of multiple-field $^{25}$Mg, $^{91}$Zr, and $^{95}$Mo solid-state NMR spectra (Figure 3) to extract the chemical shifts and EFG tensor parameters of all the metal centers in the compound. Parameters used to simulate the spectra are listed in Table S2 in the Supporting Information. To aid in the simulation of the complex $^{95}$Mo spectra, containing three overlapping second-order lineshapes, we also acquired the higher-resolution satellite transition signals at 11.7 T. The satellite transition center band was detected using the two-dimensional one-pulse processing method.[71] A $^{95}$Mo MQMAS NMR spectrum was also acquired at 21.1 T, and confirmed the quadrupolar products obtained from the lineshape simulations. The detection of three distinct $^{95}$Mo NMR signals (see Figure 3) is in agreement with the $Pna2_1$ space group, which has atomic positions of only one type, defined as *4a* (a general position). Ruling out significant Mo vacancies, considering the unit cell (determined from Le Bail fits) and the chemical composition of $ZrMgMo_3O_{12}$, three different general atomic positions *4a* for Mo are

required. This results in $ZrMgMo_3O_{12}$ for the unit cell composition. When the EFG tensor parameters, listed in Table S2 in the Supporting Information, are compared to those obtained for the same elements in other compounds,[86,87,88] it is evident that these metal sites have very small quadrupolar interactions. This finding indicates that the coordination polyhedra of the Mg, Zr, and Mo sites are nearly perfectly octahedral or tetrahedral.[89,90]

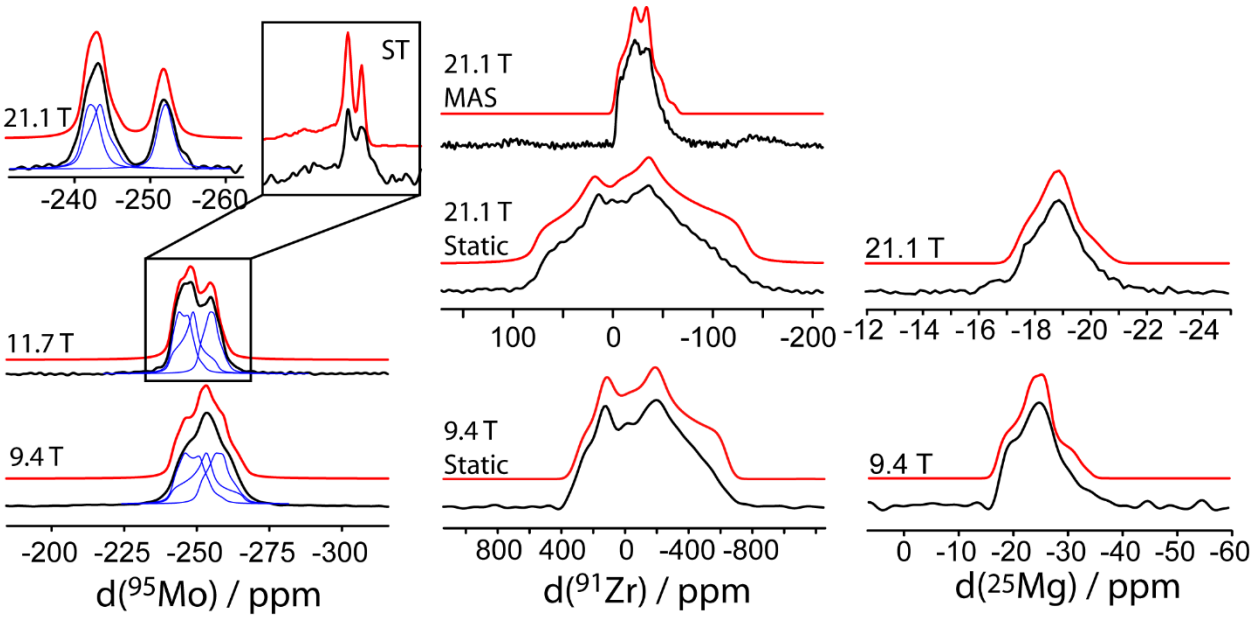


Figure 3. $^{95}$Mo MAS NMR spectra (left) acquired at applied magnetic fields of 9.4, 11.7, and 21.1 T. The inset shows the satellite transition sidebands from the 11.7 T spectrum generated using the TOP method. The $^{91}$Zr static and MAS NMR spectra acquired at 9.4 and 21.1 T are shown in the middle panel. The $^{25}$Mg MAS NMR spectra acquired at 9.4 and 21.1 T are shown on the right. In all cases the experimental spectra are shown in black (lower) and the simulations are shown in red (above). For the $^{95}$Mo NMR, the blue curves show the deconvolution of the three Mo sites.

To further refine the DFT-refined crystal structure of $ZrMgMo_3O_{12}$ and to correct any potential inaccuracies in the distortion of the polyhedra, we sought to include the experimental EFG tensor components as constraints in the refinement. As discussed above, the EFG tensor parameters are very well reproduced using PAW DFT calculations once the appropriate scaling factor is taken into consideration. The quality of a trial crystal structure can then be assessed

experimentally using a cost function ($\chi^2$) defined as follows:[54]

$$\chi^2 = \sum_{S=1}^{N}\sum_{i=1}^{3}\left(\frac{\frac{V_{ii}^{(S)calc}}{\alpha} - V_{ii}^{(S)exp}}{\sigma}\right)^2 + \left(\frac{E - E^{opt}}{\beta}\right)^2 . \quad (2)$$

In the above expression, $V_{ii}^{(S)calc}$ is a calculated EFG tensor component for nucleus $S$ (out of $N$ nuclei) and $V_{ii}^{(S)exp}$ is the corresponding experimental value. Here $\alpha$ is the scaling factor for $V_{ii}^{(S)exp}$ (see above) and $\sigma$ is the experimental uncertainty in $V_{ii}^{(S)exp}$. A DFT energy term is also included to avoid over fitting the NMR data; $E$ is the DFT energy of a trial structure, $E^{opt}$ is the energy of the minimum energy structure and $\beta$ is an experimentally optimized parameter of 0.0004 eV.[54]

To ensure that the NMR-refined structural parameters provided a good fit to the XRD data, a follow-up Rietveld refinement was carried out using these parameters as initial values; this Rietveld plot is shown in Figure S12 (c). Only the cation positions were refined while the oxygen positions were held constant. This refinement confirmed the NMR structure with regular metal-oxygen polyhedra and no unreasonable bond distances. The refined site occupancies for the Zr and Mg sites were unity within error indicating that there is no $Zr^{4+}$–$Mg^{2+}$ mixing present.

There is a significant decrease in $\chi^2$ from the FOX structure ($\chi^2 = 2.04 \times 10^{12}$) to the initial Rietveld-refined structure ($\chi^2 = 1.21 \times 10^{12}$), the follow-up Rietveld refined structure ($\chi^2 = 8.08 \times 10^{8}$) and to the DFT-refined structure ($\chi^2 = 934.5$) (see Table S3 in the Supporting Information), showing how sensitive the EFGs are to the fine details of the structure. The NMR refinement resulted in a final reduction of $\chi^2$ to 613.1. There is an overall root-mean-square deviation (RMSD) improvement in the coordinates from 0.5 ± 0.2[††] Å for the FOX coordinates,

[††] Uncertainty corresponds to the standard deviation of the RMSD of the five FOX structures.

to 0.24 Å for the inital Rietveld coordinates, to 0.029 Å for the follow-up Rietveld coordinates and 0.0014 Å for the DFT coordinates, in accord with the improvements in the $\chi^2$ parameter. A graphical comparison of the quality of the predicted EFG tensor components is shown in Figure S13 in the Supporting Information. The FOX-derived preliminary Rietveld structure grossly overestimates the size of the EFG tensor components due to its unnatural polyhedral distortions. There is a great improvement in the DFT-refined structure and further improvement with the NMR-refined structure. It can be seen that the quality of the correlation plot is comparable to those from the calibration compounds, showing that the quality of the NMR-refined crystal structure is similar to what can be obtained using single-crystal X-ray diffraction. The NMR-refined structure is shown in Figure 4, and the fractional coordinates for the atoms are given in Table S4 in the Supporting Information.

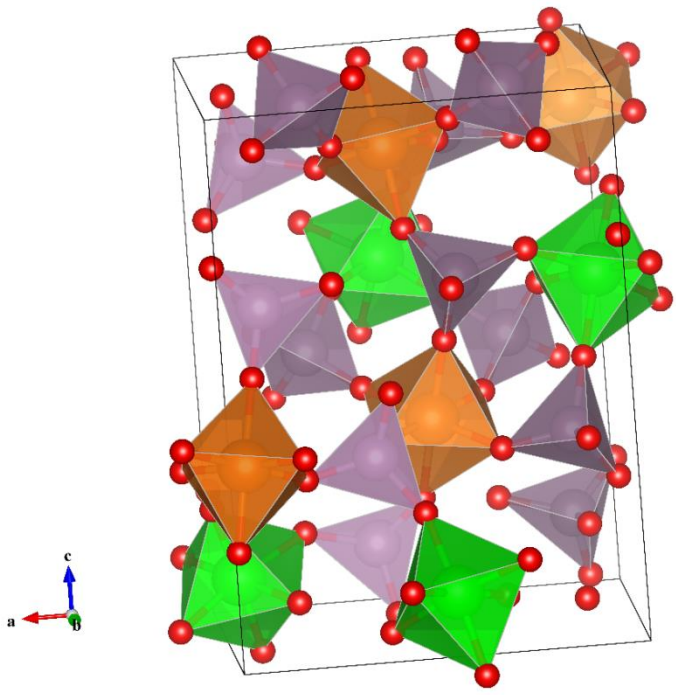


Figure 4: The NMR-refined structure of $ZrMgMo_3O_{12}$. O atoms are shown in red, $MgO_6$ coordination polyhedra in orange, $ZrO_6$ in green, and $MoO_4$ tetrahedra shown in purple. An alternative view of the structure, emphasizing the positions of the $Mg^{2+}$ cations, is shown in

Figure S14 in the Supporting Information.

Although experimental data were used to solve and refine this crystal structure, it is important to cross-validate the model structure to determine whether the data were over-fit.[54] This is typically done in diffraction experiments[91,92] and protein NMR structure solutions[93] by repeating the refinement process while omitting some of the data. Due to the paucity of NMR data in this case, and the computational demand of this approach, it is valuable here to validate the crystal structure using data that had been completely excluded from the refinement process. In this case, the $^{17}$O NMR data, omitted from the refinement process, were used for cross-validation purposes since the $^{17}$O chemical shifts are well known as being very sensitive to the distance between the oxygen and the cations.[94]

**Structure Validation by $^{17}$O NMR.** The $^{17}$O MAS ($B_0$ = 21.1 T) and MQMAS ($B_0$ = 16.4 T) NMR spectra are shown in Figure 5; there are two general chemical shift regions containing multiple resonances. One group, centered around 630 ppm, features three resonances that, once deconvoluted, integrate to line intensities of 2.9, 0.8 and 2.5, in order of decreasing chemical shift. The second group, centered at 480 ppm, has four identifiable resonances with integrated intensities of 0.97, 1.92, 1.99, and 0.98. The observation of two groups of resonances, whose integrated intensities suggest the presence of six oxygen sites in each group, is compatible with the proposed structural model. Using GIPAW DFT calculations we assign the lower chemical shift sites to the oxygen sites that are coordinated to zirconium whereas the sites with the higher chemical shifts are coordinated to magnesium.

Since $O^{2-}$ has a filled valence shell, it has a nearly spherical electron distribution that would not generate a large EFG; indeed, the oxygen sites under consideration presently have very small $^{17}$O quadrupolar coupling constants and thus neither the chemical shift values nor the

quadrupolar coupling constants can be determined precisely by lineshape fitting of a single spectrum. The center of gravity of the resonances, however, depends on the inverse square of the Larmor frequency, so by acquiring a series of $^{17}$O MAS NMR spectra at various magnetic field strengths, here 9.4, 16.4, and 21.1 T, including MQMAS data at 16.4 T, it was possible to extract the isotropic chemical shift values and quadrupolar products ($P_Q = C_Q(1+\eta^2/3)^{1/2}$) for all sites. The apparent chemical shifts plotted as a function of the inverse square of the Larmor frequency is a linear function and the intercept is the isotropic chemical shift.[95] The $P_Q$ value can be extracted from the slope of the graphs as $(\text{slope}/-6000)^{1/2}$. To include the MQMAS data it was necessary to use the universal chemical shift referencing method of Amoureux[96] and scale the Larmor frequency by −10/17.[95] The $^{17}$O MAS and MQMAS NMR spectra are shown in Figure 5, and Figure S15 (see Supporting Information), linear fits of the of the magnetic field dependence of the peak positions are shown in Figure S16 in the Supporting Information, and the extracted $\delta_{iso}$ and $P_Q$ values are listed in Table S2 in the Supporting Information.

The oxygens bound to magnesium have smaller quadrupolar products of 1.3 MHz whereas oxygens bound to zirconium have $P_Q$ values of 1.8 to 2.0 MHz. This is in agreement with the oxygens having a more covalent interaction with zirconium than magnesium, thus altering the spherical symmetry of the $O^{2-}$ anion and increasing the $P_Q$. The plots in Figure S16 show the correlation between the calculated and experimental quadrupolar products as well as chemical shifts. There is a very good agreement between the calculated and experimental values for both parameters. The slope of best fit for the $P_Q$ products is 1.04 which is very close to the expected slope of 1.029 ± 0.007 from the calibration, and the $P_Q$ values are slightly better reproduced using the NMR-refined structure ($R^2$ = 0.9979) than the DFT-refined structure ($R^2$ = 0.9976). This represents a 14 % decrease in the unexplained variance of the $P_Q$ data between the

NMR-refined and DFT-refined structure.

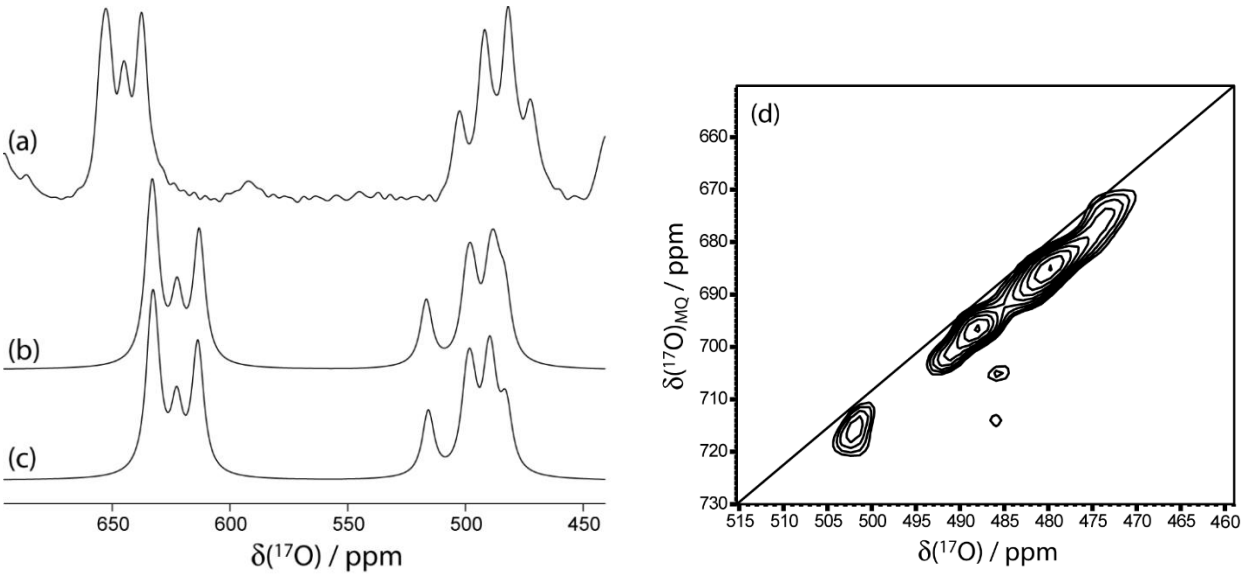


Figure 5. The $^{17}$O MAS NMR spectrum (a) acquired at 21.1 T with (b) the predicted $^{17}$O NMR spectra using the DFT-refined structure and (c) from the NMR-refined structure. The MQMAS NMR spectrum acquired at 16.4 T is shown in (d). Plots correlating the apparent shifts as a function of the inverse of the squared Larmor frequency are shown in Figure S15 in the Supporting Information. Correlations between the calculated and experimental $P_Q$ and $\delta_{iso}$ values are shown in Figure S16 in the Supporting Information.

Although the relative shifts for each of the two groups of resonances were well reproduced, the $^{17}$O chemical shifts were not reproduced quantitatively. However, it is well known that spin-orbit induced relativistic effects (heavy atom, light atom effect, HALA) can have a large impact on the chemical shifts of lighter elements.[97] We performed cluster model DFT calculations using the two-component ZORA method to include scalar and spin-orbit relativistic effects. These calculations predict a −53 ppm relativistic shift for the oxygen sites connected to a Mo and a Zr site, but only −34 ppm for those connected to Mo and Mg. The *ad hoc* incorporation of this relativistic shift with the GIPAW results (see Figure S16) improves the slope from 0.7 to 0.8 and improves the correlation coefficient from 0.9946 to 0.9975. It is

expected that full, four-component, relativistic DFT calculations would further improve the slope of the plot. Also, as was the case with the $P_Q$ values, the isotropic chemical shifts are better reproduced by the NMR-refined structure than the DFT-refined structure, which gives a correlation coefficient of 0.9967.

The improvement in the predicted $^{17}O$ NMR spectra can also be seen from Figure 5. The spread of the high-chemical-shift resonances is smaller in the spectrum of the NMR-refined structure and the experimental spectrum. The lowest chemical shift resonance, which should not be observable according to the DFT-refined structure, is visible in the NMR spectrum predicted from the NMR-refined crystal structure. The quality of the correlations in Figures S13 and S16 in the Supporting Information demonstrates the high quality of the final NMR-refined crystal structure. These also show that DFT-based crystal structure refinements can be improved by the explicit inclusion of experimental data, such as EFG tensor components, which would lead to more accurate information concerning polyhedral distortions, which are especially important here.

**Phonon Modes.** As an additional step in validating the structure, and in consideration of the importance of dynamics[2,31,79,98] in framework materials, the $\Gamma$-point optic phonon frequencies were calculated using CASTEP (see Table S5 in the Supporting Information). The frequencies were corrected for errors due to finite sampling on the effective charges by imposition of the acoustic sum rule. The calculated $\Gamma$-point optic phonon frequencies of $ZrMgMo_3O_{12}$, compared to those previously reported for $Y_2Mo_3O_{12}$,[79] show an increased number of modes below 50 $cm^{-1}$ but otherwise a general increase in mode energies.

All of the $ZrMgMo_3O_{12}$ modes are Raman-active, and therefore the calculated modes can be compared to experiment (Figure 6). Approximate assignments of vibrational modes are based

on studies of $Y_2Mo_3O_{12}$ and $Al_2W_3O_{12}$.[99, 100] Of special interest are the modes below about 200 $cm^{-1}$, which include the librational optic modes that have been related to quasi-rigid unit rotations and NTE.[35] The low-energy modes in $ZrMgMo_3O_{12}$ have similar relative intensities to what is observed for $Al_2W_3O_{12}$,[100] but have much higher relative intensities than for $Y_2Mo_3O_{12}$.[79] The similarity of the Raman spectra of $ZrMgMo_3O_{12}$ and $A_2M_3O_{12}$ materials suggests similar dynamics and potentially a similar mechanism of thermal expansion reduction. The calculated Raman-active modes replicate the observed librational, translational, and bending mode energies well, but predict a smaller spread of stretching-mode energies than observed.

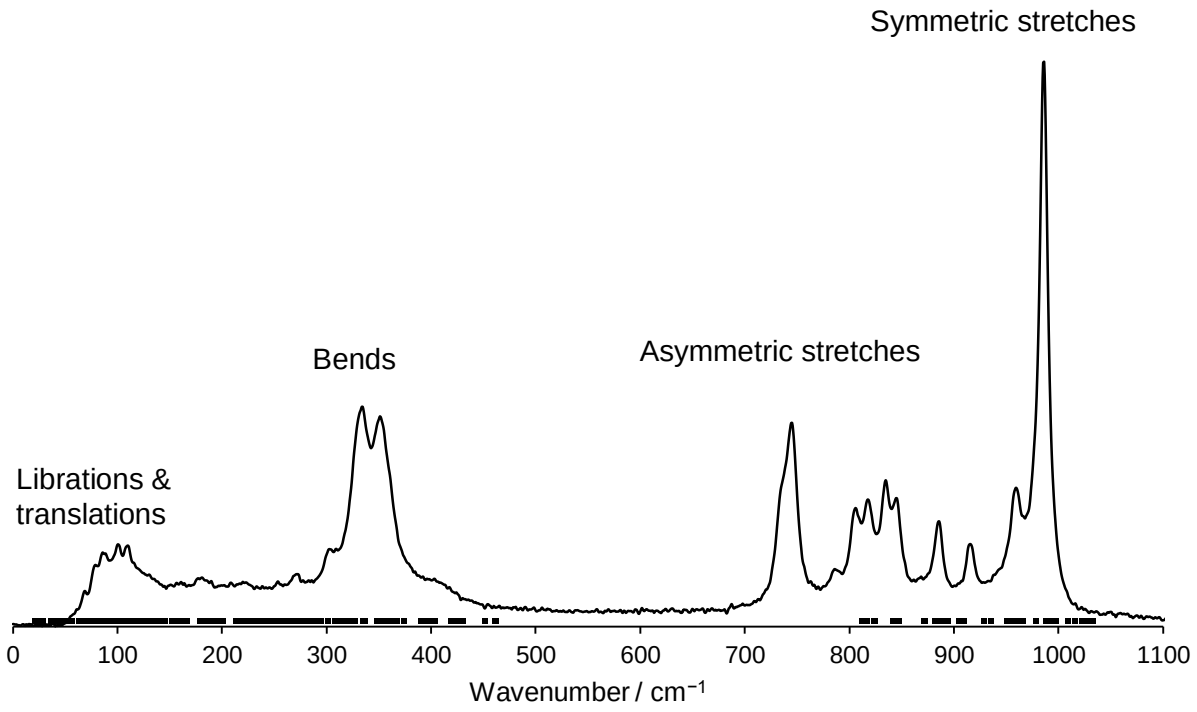


Figure 6: The experimentally-determined Raman spectrum of $ZrMgMo_3O_{12}$. Calculated Γ-point optic phonon frequencies are shown as (▪).

**Conductivity.** $ZrMgMo_3O_{12}$ shows significant conductivity, $4.1 \times 10^{-4}$ $\Omega^{-1}$ $m^{-1}$ at 520 °C (see Figures S17 and S18 in the Supporting Information); this level of conductivity in an insulating solid indicates a considerable ionic conductivity, as was previously reported in the structurally related material $HfMgW_3O_{12}$,[26] although several orders of magnitude less than fast ionic conductors.[101] The Nyquist plots (Figure S17) indicate only one time constant, consistent with a single species as the major contributor to the conductivity. Ionic conductivity is not surprising given the crystal structure; if the $Mg^{2+}$ ions are mobile the structure can be viewed as a network of $ZrO_6$ and $MoO_4$ polyhedra with $Mg^{2+}$ in cavities that are connected along several directions (see Figure S14). The conductivity of $ZrMgMo_3O_{12}$ is significantly lower than was reported for $HfMgW_3O_{12}$;[26] it falls within the range of conductivities of $A^{3+}$ ions in $A_2M_3O_{12}$ materials such as $Al_2W_3O_{12}$ and $Sc_2Mo_3O_{12}$.[102] The activation energy for ionic conductivity in $ZrMgMo_3O_{12}$ was determined to be 82 kJ $mol^{-1}$ (Figure S18), which is close to that of $HfMgW_3O_{12}$ (80.6 kJ $mol^{-1}$)[26] and the fast ion conductor $LiAlSiO_4$ (81 kJ $mol^{-1}$).[101]

**Correlation of Structure and Properties.** The orthorhombic $Pna2_1$ structure of $ZrMgMo_3O_{12}$ (Figure 4) is related to the *Pbcn* $Sc_2W_3O_{12}$ structure with the $Zr^{4+}$ and $Mg^{2+}$ ions associated with the $Sc^{3+}$ sites. In Figures 7 and 8, structure and bonding features of all orthorhombic $A_2M_3O_{12}$ structures of sufficient quality from the literature are compared to $ZrMgMo_3O_{12}$. Sources of structural data and CTEs are given in Table 1.

Table 1: Intrinsic CTEs and structures from the literature of materials in the orthorhombic *Pbcn* $Sc_2W_3O_{12}$ structure and $ZrMgMo_3O_{12}$.

| Material | $\alpha_\ell$ / $10^{-6}$ $K^{-1}$ | Temperature range of measurement of $\alpha_\ell$ / °C | Structure determination method | References |
|---|---|---|---|---|
| $Al_2Mo_3O_{12}$ | 2.4 | 250 to 650 | Neutron powder diffraction | 103, 104 |
| $Al_2W_3O_{12}$ | 2.1 | 50 to 550 | Neutron powder diffraction | 105, 106 |
| $Fe_2Mo_3O_{12}$ | 1.8 | 550 to 750 | Neutron powder diffraction | 103, 104 |
| $Cr_2Mo_3O_{12}$ | 0.7 | 400 to 750 | Synchrotron XRPD | 104 |

| | | | | |
|---|---|---|---|---|
| **$ZrMgMo_3O_{12}$** | **0.16** | **25 to 450** | **NMR crystallography** | **Current work** |
| $In_2Mo_3O_{12}$ | −1.9 | 370 to 760 | Synchrotron XRPD | 32 |
| $Sc_2Mo_3O_{12}$ | −2.1 | −93 to 27 | Single-crystal XRD | 107, 108 |
| $Sc_2W_3O_{12}$ | −2.2 | −263 to 176 | Single-crystal XRD | 30, 107 |
| $Lu_2Mo_3O_{12}$ | −6.0 | 25 to 700 | Synchrotron XRPD | 109, 110 |
| $Y_2W_3O_{12}$ | −7.0 | 20 to 800 | Neutron powder diffraction | 105 |
| $Er_2Mo_3O_{12}$ | −7.6 | 25 to 700 | Synchrotron XRPD | 109, 110 |
| $Y_2Mo_3O_{12}$ | −9.0 | −263 to 176 | Synchrotron XRPD | 31 |

The reduction in symmetry from *Pbcn* (space group number 60) to $Pna2_1$ (space group number 33) leads to the addition of one crystallographically distinct Mo site and six O sites, as well as the splitting of the *A* site into a Zr site and a Mg site. This in turn allows a greater variation in the distribution of *M*-O-*A* angles compared to the *Pbcn* orthorhombic phases of $A_2M_3O_{12}$ materials (Figure 7). The *M*-O-*A* bond angle distribution of $ZrMgMo_3O_{12}$ is the broadest yet reported for this family of materials. Not all the materials in this family follow the same trend regarding average *M*-O-*A* bond angle, but they can be separated into three groups of materials with similar properties (Figure 7, and Figure S19 in the Supporting Information). The average *M*-O-*A* angles of the molybdate $A_2M_3O_{12}$ materials and $ZrMgMo_3O_{12}$ are remarkably consistent; all fall within 1.5° of 156.6°. By contrast, the $A_2W_3O_{12}$ materials trend towards increasing average *M*-O-*A* angle with increasingly negative thermal expansion. The $A_2Mo_3O_{12}$ materials that are orthorhombic at room temperature (Figure 7) show decreasing *M*-O-*A* angle spread with increasing NTE, while those that are monoclinic at room temperature (Figure S19(a)) show relatively consistent angles with changing CTE. The high *M*-O-*A* angle range for $ZrMgMo_3O_{12}$ correlates with both to its low orthorhombic-monoclinic phase transition temperature and its zero thermal expansion.

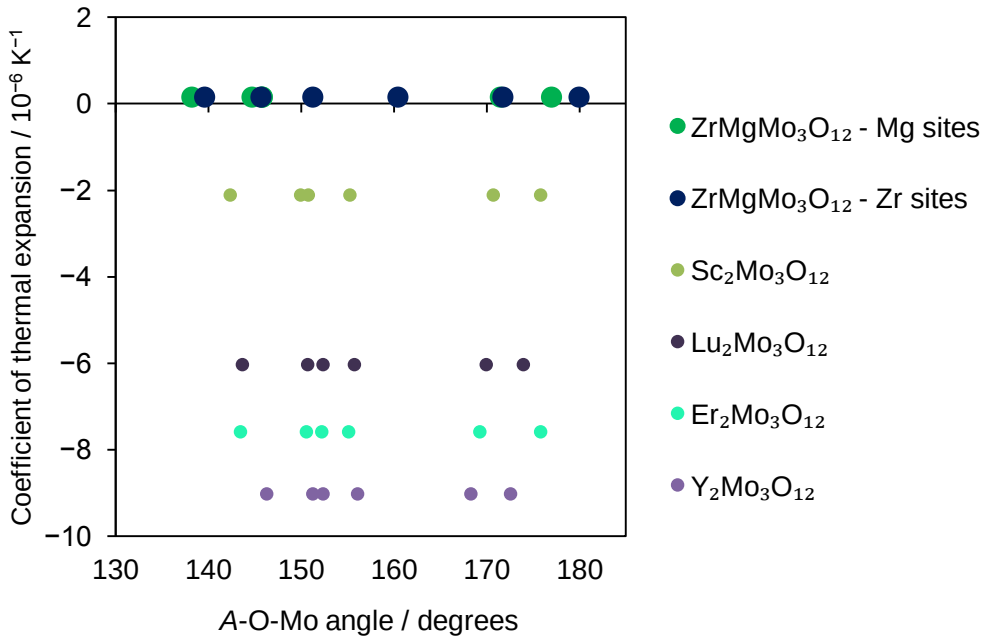


Figure 7: Correlation of CTE in the *Pbcn* orthorhombic phase of $A_2Mo_3O_{12}$ materials with *M*-O-*A*/Mg bond angles for $ZrMgMo_3O_{12}$ (large symbols) and $A_2Mo_3O_{12}$ materials that are stable in the *Pbcn* orthorhombic space group at room temperature (see Figure S19 in the Supporting Information for other $A_2M_3O_{12}$ materials). Information for $A_2M_3O_{12}$ materials were taken from the literature; see Table 1 for complete references.

Inherent distortions (*i.e.*, distortions at the lowest temperature where data are available) of $AO_6$ polyhedra in $ZrMgMo_3O_{12}$ and $A_2M_3O_{12}$ materials, as calculated by IVTON,[111] are shown in Figure 8. The negative correlation of the CTE with polyhedral distortion is clearly visible for the $A_2Mo_3O_{12}$ materials, while the average distortion value for $ZrO_6$ and $MgO_6$ polyhedra is higher than would be expected from its CTE, as the average distortion value is close to that of $Sc_2Mo_3O_{12}$. The $MgO_6$ octahedron has an inherent distortion close to what would be expected from the CTE.

$AO_6$ distortion in $ZrMgMo_3O_{12}$ is largely related to variance of the O-*A*-O angles within the octahedra, as is common in $A_2M_3O_{12}$ materials (see Figure S20 in the Supporting Information). To determine the causes of zero thermal expansion in $ZrMgMo_3O_{12}$ one must

consider both the origins of the polyhedral distortion in $ZrMgMo_3O_{12}$ and how much the polyhedra would be expected to distort with increasing temperature.

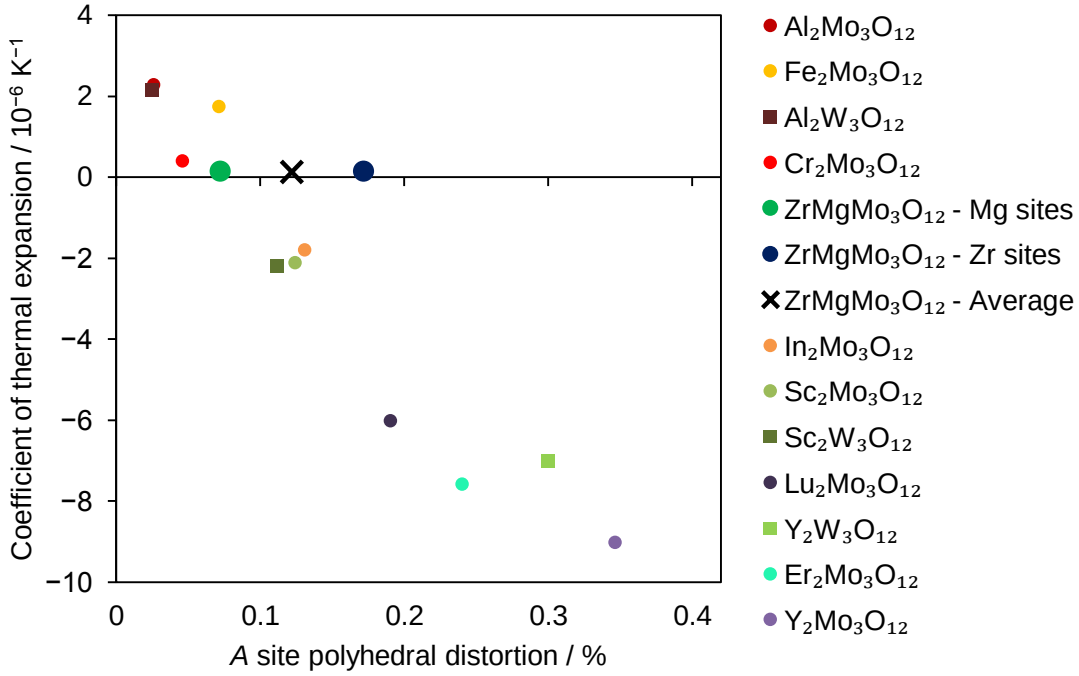


(a)

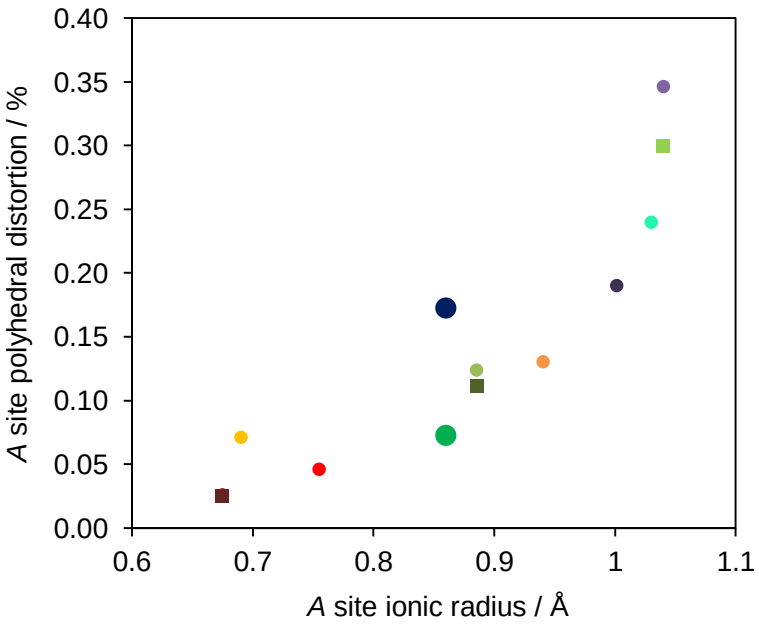


(b)

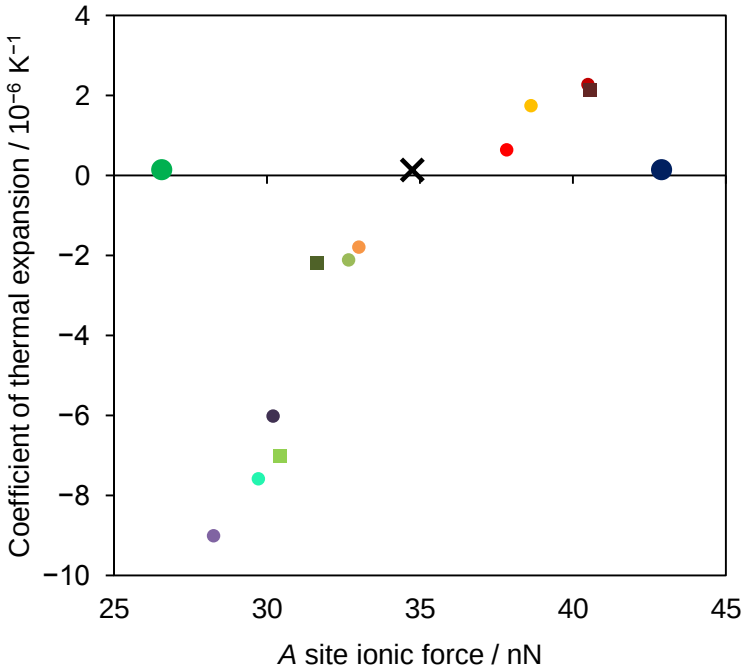


(c)

Figure 8: Coefficients of thermal expansion as a function of (a) inherent polyhedral ($AO_6$) distortion in $ZrMgMo_3O_{12}$ (large symbols) and $A_2M_3O_{12}$ materials, (b) inherent polyhedral distortion ($AO_6$) in $ZrMgMo_3O_{12}$ and $A_2M_3O_{12}$ materials as a function of the Shannon ionic radii of the *A* site cations[112] (inherent polyhedral distortions of $AlO_6$ in $Al_2Mo_3O_{12}$ and $Al_2W_3O_{12}$ are nearly identical and these two points overlap), and (c) coefficients of thermal expansion of $ZrMgMo_3O_{12}$ (large symbols) and $A_2M_3O_{12}$ materials as a function of their *A* site ionic force. Structures of $A_2M_3O_{12}$ materials were taken from the literature; see Table 1 for references.

Polyhedral distortion in $A_2M_3O_{12}$ materials is generally correlated with the Shannon ionic radius[112] of the *A* cation, as shown in Figure 8 (b), with larger cations permitting and/or causing larger polyhedral distortions. However, $Zr^{4+}$ and $Mg^{2+}$ have nearly identical radii yet very different levels of polyhedral distortion, with $Mg^{2+}$ close to the trend for $A_2M_3O_{12}$ materials. A very large inherent distortion (19.8 %) in $ZrO_6$ octahedra was found in $ZrW_2O_8$,[31] but this distortion is essentially static and the NTE mechanism in $ZrW_2O_8$ does not involve distortion of the rigid polyhedra. It is therefore plausible that the distortion of the $ZrO_6$ octahedra in $ZrMgMo_3O_{12}$ is also static. The inherent polyhedral distortion for $A_2M_3O_{12}$ materials increases

nonlinearly with increasing ionic radius. This nonlinearity could be related to the instability of the orthorhombic $Sc_2W_3O_{12}$ structure above a critical *A* cationic radius; $A_2W_3O_{12}$ materials with *A* greater in size than $Ho^{3+}$ (104.1 pm) and $A_2Mo_3O_{12}$ materials with *A* greater in size than $Y^{3+}$ (104 pm) crystallize in a variety of structures different from that of $Sc_2W_3O_{12}$.[113,114]

The ease of distortion of the $AO_6$ polyhedra could be rationalized, more fundamentally, in terms of the magnitude of the attractive forces ($F_a$) between the $A^{2+/3+/4+}$ cation and the $O^{2-}$ anion. To estimate this attractive force, and the consequent ease of distortion of the $ZrO_6$, $MgO_6$ and other octahedra, the ionic attractive force,[115] expressed as $-k_eZ_+Z_-e^2/r_o^2$ where $k_e$ is Coulomb's constant, $Z_+$ is the valence of the cation, $Z_-$ is the average valence of the anions, $e$ is the elementary charge and $r_o$ is the sum of the cation and anion radii,[112] can be used. Instead of using standard valences, these attractive forces were calculated using the bond valence method[116] within IVTON.[111] Inherent polyhedral distortion is expressed as a function of the ionic attractive force in Figure S21 (see Supporting Information), showing that the inherent distortions of the $ZrO_6$ and $MgO_6$ polyhedra are highly different from $A^{3+}O_6$ polyhedra for $A_2M_3O_{12}$ materials. However, estimating their average effect, together they could act like a conventional *A* site.

Coefficients of thermal expansion of $A_2M_3O_{12}$ materials and $ZrMgMo_3O_{12}$ are shown as a function of their *A* site ionic force in Figure 8 (c).[‡‡] The general trend is increased CTE with increased ionic force. A clear difference is visible upon comparison of Figure 8 (c) to Figure 8 (a): $ZrMgMo_3O_{12}$, $Fe_2Mo_3O_{12}$, and $Er_2Mo_3O_{12}$ fit the *A* site ionic force trends better, suggesting

[‡‡] Instead of using the sum of Shannon ionic radii to calculate the interatomic distance and thereby the cationic force, average crystallographic *A*-O bond distances could have been used. This gives a poorer correlation to the CTEs of the compounds (Figure S22 in the Supporting Information), especially at the extremes of thermal expansion of the data set. This could be due to the underestimation of bond lengths in thermomiotic materials as measured by diffraction, due to the librational motion of the oxygen atoms, which, when time-averaged over the course of a diffraction experiment, reduces the apparent bond lengths.[5]

that the ionic force offers a good estimate of the distortability of the $AO_6$ polyhedron for $A_2M_3O_{12}$ materials and $ZrMgMo_3O_{12}$, and that the zero thermal expansion behaviour of $ZrMgMo_3O_{12}$ is due to a mixed effect from the more rigid $ZrO_6$ octahedra and the more distortable $MgO_6$ octahedra.

This assertion regarding the polyhedral rigidity of $ZrMgMo_3O_{12}$ is supported by other physical properties discussed above, including the presence of low-frequency optic modes in the Raman spectrum and the calculated vibrational spectrum, and the measured bulk modulus. Specifically, the bulk modulus of orthorhombic $ZrMgMo_3O_{12}$ (31 ± 3 GPa) is less than that of orthorhombic $Al_2W_3O_{12}$ (48 GPa),[117] similar to that of orthorhombic $Sc_2Mo_3O_{12}$ (32 ± 2 GPa)[117] and $Sc_2W_3O_{12}$ (31 ± 3 GPa),[118] and greater than that of orthorhombic $Y_2W_3O_{12}$ (27 GPa)[119] and $Y_2Mo_3O_{12}$ (21 ± 3 GPa),[79] indicating that the overall rigidity of $ZrMgMo_3O_{12}$ is close to what would be expected given its CTE.

The absence of significant hygroscopicity in $ZrMgMo_3O_{12}$ can also be explained through knowledge of its structure. The atomic packing fractions of $ZrMgMo_3O_{12}$ and $A_2M_3O_{12}$ materials are shown in Figure S23 (see Supporting Information); the packing fraction of $ZrMgMo_3O_{12}$ (0.17) is larger than for $A_2M_3O_{12}$ materials that are known to incorporate water into their crystal structures[31,113,119] and is close to those of the non-hygroscopic $A_2M_3O_{12}$ materials $Sc_2Mo_3O_{12}$ and $In_2Mo_3O_{12}$.

## CONCLUSIONS

We have shown that $ZrMgMo_3O_{12}$ is a zero thermal expansion material. It is thermally stable in its orthorhombic phase from −125 °C to 700 °C. Unlike some members of the $A_2M_3O_{12}$ family, it is not hygroscopic.

The bulk average value of the linear thermal expansion coefficient, as determined from dilatometry, is $\alpha_\ell = (-3 \pm 1) \times 10^{-7}\ K^{-1}$ from 23 °C to 500 °C. The average linear intrinsic CTE, as determined by X-ray diffraction, also is very close to zero: $\alpha_\ell = (1.6 \pm 0.2) \times 10^{-7}\ K^{-1}$ from 25 °C to 450 °C and $\alpha_\ell = (9 \pm 3) \times 10^{-7}\ K^{-1}$ from 450 to 700 °C. The small differences between intrinsic and extrinsic thermal expansion at lower temperatures are probably due to microstructure, and especially behaviour of microcracks. Nevertheless, the average linear CTE is exceptionally small over a wide temperature range. However, the CTE is anisotropic, with the maximum difference between two axial CTEs for $ZrMgMo_3O_{12}$ between 25 °C and 450 °C, $\Delta\alpha_{max}$, being $12.3 \times 10^{-6}\ K^{-1}$.

The structure of $ZrMgMo_3O_{12}$, intractable by X-ray powder diffraction and not feasible by single crystal X-ray diffraction, was determined here by NMR crystallography. We made use of NMR activity of all the nuclei, $^{91}Zr$, $^{25}Mg$, $^{95}Mo$, and $^{17}O$, where the $^{17}O$ results were excluded from the initial analysis to allow independent validation of the overall structure. In order to obtain the $^{17}O$ NMR, a synthesis method for $^{17}O$-enriched $MoO_3$ was developed. Overall, the quality of the NMR-refined crystal structure is similar to what can be obtained using single-crystal X-ray diffraction. The space group of the orthorhombic phase of $ZrMgMo_3O_{12}$ is $Pna2_1$ and its structure is related to the structure of $Sc_2W_3O_{12}$ with ordering of $Mg^{2+}$ and $Zr^{4+}$ cations. The structure suggests the possibility of ionic conductivity, which was confirmed

experimentally. The solution of the structure of $ZrMgMo_3O_{12}$ should aid in the structure determination of other $AMgM_3O_{12}$ materials with interesting thermal expansion properties.

The calculated and experimental Raman spectra both indicate a high density of low-frequency modes associated with librations of quasi-rigid units that could play a role in negative thermal expansion in this framework structure. Velocity of sound measurements revealed low bulk and shear moduli relative to conventional oxide ceramics, again supporting flexibility of the linked polyhedra.

Compared with the orthorhombic phases of $A_2M_3O_{12}$ materials, $ZrMgMo_3O_{12}$ shows the broadest distribution of *M*-O-*A* angles yet reported. While the average inherent distortion of $AO_6$ polyhedra in $ZrMgMo_3O_{12}$ is similar to that of materials with negative, rather than near-zero CTEs, distortion of the $MgO_6$ octahedra alone is a better predictor of the average CTE. The distortion in $ZrO_6$ is likely static in nature. We found that the average *A*-site ionic force in both $ZrMgMo_3O_{12}$ and in a wide range of $A_2M_3O_{12}$ materials is a useful predictor of the CTE. Therefore, we have been able to use the crystal structure to understand the properties of $ZrMgMo_3O_{12}$, providing further experimental validation of the structure. The current work provides a compelling example of the value of NMR crystallography in providing structures of sufficient accuracy to enable quantitative insights concerning the behaviour of a material.

## ACKNOWLEDGEMENTS

F. A. Perras thanks the Natural Sciences and Engineering Research Council (NSERC) of Canada for a graduate scholarship. M. Bieringer, D. L. Bryce, M. A. White and J. W. Zwanziger thank NSERC for funding. Access to the 21.1 T NMR spectrometer was provided by the National Ultrahigh-Field NMR Facility for Solids (Ottawa, Canada), a national research facility funded by

a consortium of Canadian Universities and Bruker BioSpin, and managed by the University of Ottawa (http://nmr900.ca). Acknowledgment is made to the donors of The American Chemical Society Petroleum Research Fund for partial support of this research (grant to D. L. B.). C. P. Romao thanks the Sumner Foundation for a graduate scholarship. M. Bieringer, M. A. White and J. W. Zwanziger acknowledge support from the Canada Foundation for Innovation. B. A. Marinkovic is grateful to CNPq (National Council for Scientific and Technological Development) for a Research Productivity Grant. We appreciate the assistance of D. P. Bishop and S. Corbin (dilatometry), M. Johnson (DSC), and M. Obrovac and J. Dahn (ball milling).

## SUPPORTING INFORMATION DESCRIPTION

Supporting Information. Experimental details, detailed materials characterization and results (phase stability, thermal expansion, structure determination by NMR crystallography, structure validation by $^{17}O$ NMR, phonon modes, conductivity, correlation between structure and properties). This material is available free of charge via the Internet at http://pubs.acs.org.

**TABLE OF CONTENTS GRAPHIC**

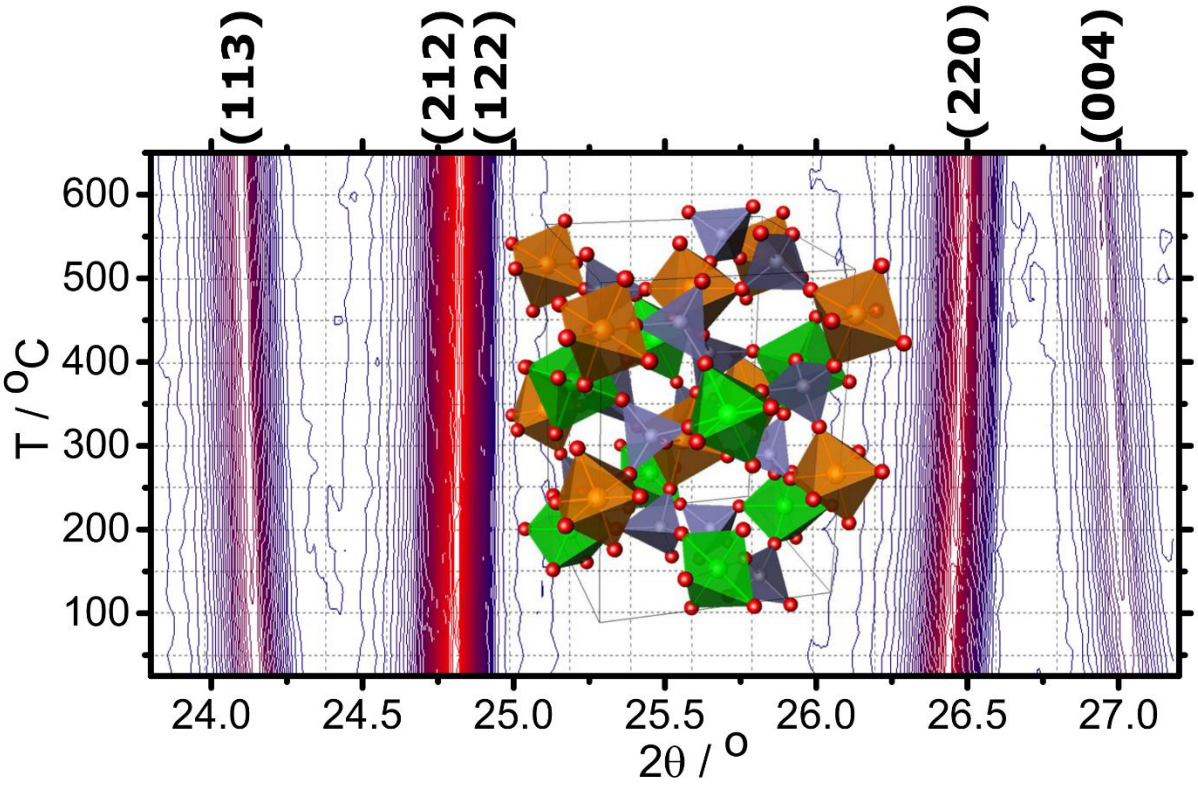


**REFERENCES**


1. Mary, T. A.; Evans, J. S. O.; Vogt, T.; Sleight, A. W. *Science* **1996**, *272* , 90–92.

2. For a recent comprehensive review, see Romao, C. P.; Miller, K. J.; Whitman, C. A.; White, M. A.; Marinkovic, B. A. Negative Thermal Expansion (Thermomiotic) Materials. In *Comprehensive Inorganic Chemistry II*; Reedijk, J.; Poeppelmeier, K., Ed.; Elsevier: Oxford, UK, 2013; Vol. 4, p 128–51.

3. Miller, W.; Smith, C. W.; Mackenzie, D. S.; Evans, K. E. *J. Mater. Sci.* **2009**, *44*, 5441–5451.

4. Lind, C. *Materials* **2012**, *5*, 1125–1154.

5. Barrera, G.D.; Bruno, J. A. O.; Barron T. H. K.; Allan, N. L. *J. Phys. Condens. Matter* **2005**, *17*, R217–R252.

6. Hu, L.; Chen, J.; Fan, L. L.; Ren, Y.; Rong, Y. C.; Pan, Z.; Deng, J. X.; Yu, R. B.; Xing, X. R., *J. Am. Chem. Soc.* **2014**, *136*, 13566–1569.

7. Sullivan, L. M.; Lukehart, C. M. *Chem. Mater.* **2005**, 2136–2141.

8. Sun, L.; Sneller, A.; Kwon, P. *Compos. Sci. Technol.* **2008**, *68*, 3425–30.

9. Holzer, H.; Dunand, D. C. *J. Mater. Res.* **1999**, *14*, 780–789.

10. Morelock, C. R.; Greve, B. K.; Cetinkol, M.; Chapman, K. W.; Chupas, P. J.; Wilkinson, A. P. *Chem. Mater*. **2013**, *25*, 1900–1904.

11. Carey, T.; Tang, C. C.; Hriljac, J. A.; Anderson, P. A. *Chem. Mater.* **2014**, *26*, 1561–1566.

12. Phillips, A. E.; Halder, G. J.; Chapman, K. W.; Goodwin, A. L.; Kepert, C. J. *J. Am. Chem. Soc.* **2010**, *132*, 10–11.

13. Tokoro, H.; Nakagawa, K.; Imoto, K.; Hakoe, F.; Okoshi, S.-I. *Chem. Mater.* **2012**, *24*, 1324–1330.

14. Margadonna, S.; Prassides, K.; Fitch, A. N. *J. Am. Chem. Soc.* **2004**, *126*, 15390–15391.

15. Chen, J.; Xing, X.; Sun, C.; Hu, P.; Yu, R.; Wang, X.; Li, L. *J. Am. Chem. Soc.* **2008**, *130*, 1144–1145.

16. Takenaka, K.; Takagi, H. *Appl. Phys. Lett.* **2009**, *94*, 131904-1–131904-3.

17. Miller, K. J.; Romao, C. P.; Bieringer, M.; Marinkovic, B. A.; Prisco, L.; White, M. A. *J. Am. Ceram. Soc.* **2013**, *96*, 561–566.

18. Suzuki, T.; Omote, A. *J. Am. Ceram. Soc.* **2006**, *89*, 691–693

19. Mary, T. A.; Sleight, A. W. *J. Mater. Res.* **1999**, *14*. 912–915.

20. Launay, S.; Wallez, G.; Quarton, M. *Chem. Mater.* **2001**, *13*, 2833–2837.

21. Evans, J. S. O.; Mary, T. A.; Subramanian, M. A.; Sleight, A. W. *Chem. Mater.* **1996**, *8*, 2809–2823.

22. Pryde, A. K. A.; Hammonds, K. D.; Dove, M. T.; Heine, V.; Gale, J. D.; Warren, M. C. *J. Phys.: Condens. Matter* **1996**, *8*, 10973–10982.

23. Suzuki, T.; Omote, A. *J. Am. Ceram. Soc.* **2004**, *87*, 1365–1367.

24. Marinkovic, B. A.; Jardim, P.M.; Ari, M.; de Avillez, R. R.; Rizzo, F.; Ferreira, F. F. *Phys. stat. sol. (b)* **2008**, *245*, 2514–2519.

25. Song, W. B.; Liang, E.-J.; Liu, X.-S.; Li, Z.-Y.; Yuan, B.-H.; Wang, J.-Q. *Chin. Phys. Lett.* **2013** *30*, 126502-1–126502-4.

26. Omote, A.; Yotsuhashi, S.; Zenitani, Y.; Yamada, Y. *J. Am. Ceram. Soc.* **2011**, *94*, 2285–2288.

27. Steele, B. C. H.; Heinzel, A. *Nature*, **2001**, *414*, 345–352.

28. Gindhart, A. M.; Lind, C.; Green, M. *J. Mater. Res.* **2008**, *23*, 210–213.

29. Prisco, L. P.; Romao, C. P.; Rizzo, F.; White, M. A.; Marinkovic, B. A. *J. Mater. Sci.* **2013**, *48*, 2986–2996.

30. Evans, J. S. O.; Mary, T. A.; Sleight, A. W. *J. Solid State Chem.* **1998**, *137*, 148–160.

31. Marinkovic, B. A.; Ari, M.; de Avillez, R. R.; Rizzo, F.; Ferreira, F. F.; Miller, K. J.; Johnson, M. B.; White, M. A. *Chem. Mater.* **2009**, *21*, 2886–2894.

32. Marinkovic, B. A.; Ari, M.; Jardim, P. M.; de Avillez, R. R.; Rizzo, F.; Ferreira, F. F. *Thermochim. Acta* **2010**, *499*, 48–53.

33. Makovicky, E.; Balic-Žunić, T. *Acta Cryst. B* **1998**, *54*, 766–773.

34. Withers, R. L.; Tabira, Y.; Evans, J. S. O.; King, I. J.; Sleight, A. W. *J. Solid State Chem.* **2001**, *157*, 186–192.

35. Wang, L.; Wang, F.; Yuan, P.-F.; Sun, Q.; Liang, E.-J.; Jia, Y.; Guo, Z.-X. *Mater. Res. Bull.* **2013**, *48*, 2724–2729.

36. Harris, R. K.; R. E. Wasylishen; M. J. Duer, *NMR Crystallography*, John Wiley & Sons, Chichester, UK, **2009**.

37. Martineau, C.; Senker, J.; Taulelle, F. *Annu. Rep. NMR Spectrosc.* **2014**, *82*, 1–57.

38. Elena, B.; Emsley, L. *J. Am. Chem. Soc.* **2005**, *127*, 9140–9146.

39. Elena, B.; Pintacuda, G.; Mifsud, N.; Emsley, L. *J. Am. Chem. Soc.* **2006**, *128*, 9555–9560.

40. Pickard, C. J.; Salager, E.; Pintacuda, G.; Elena, B.; Emsley, L. *J. Am. Chem. Soc.* **2007**, *129*, 8932–8933.

41. Santos, S. M.; Rocha, J.; Mafra, L. *Cryst. Growth Des.* **2013**, *13*, 2390–2395.

42. Salager, E.; Day, G. M.; Stein, R. S.; Pickard, C. J.; Elena, B.; Emsley, L. *J. Am. Chem. Soc.* **2010**, *132*, 2564–2566.

43. Baias, M.; Widdifield, C. M.; Dumez, J.-N.; Thompson, H. P. G.; Cooper, T. G.; Salager, E.; Bassil, S.; Stein, R. S.; Lesage, A.; Day, G. M.; Emsley, L. *Phys. Chem. Chem. Phys.* **2013**, *15*, 8069–8080.

44. Brouwer, D. H.; Darton, R. J.; Morris, R. E.; Levitt, M. H. *J. Am. Chem. Soc.* **2005**, *127*, 10365–10370.

45. Brouwer, D. H.; Cadars, S.; Eckert, J.; Liu, Z.; Terasaki, O.; Chmelka, B. F. *J. Am. Chem. Soc.* **2013**, *135*, 5641–5655.

46. Bouchevreau, B.; Martineau, C.; Mellot-Draznieks, C.; Tuel, A.; Suchomel, M. R.; Trébosc, J.; Lafon, O.; Amoureux, J.-P.; Taulelle, F. *Chem. Mater.* **2013**, *25*, 2227–2242.

47. Martineau, C.; Bouchevreau, B.; Tian, Z.; Lohmeier, S.-J.; Behrens, P.; Taulelle, F. *Chem. Mater.* **2011**, *23*, 4799–4809.

48. Bouchevreau, B.; Martineau, C.; Mellot-Draznieks, C.; Tuel, A.; Suchomel, M. R.; Trébosc, J.; Lafon, O.; Amoureux, J.-P.; Taulelle, F. *Chem. Eur. J.* **2013**, *19*, 5009–5013.

49. Brouwer, D. H.; Enright, G. D.; *J. Am. Chem. Soc.* **2018**, *130*, 3095–3105.

50. Brouwer, D. H. *J. Am. Chem. Soc.* **2008**, *130*, 6306–6307.

51. Wylie, B. J.; Schwieters, C. D.; Oldfield, E.; Rienstra, C. M. *J. Am. Chem. Soc.* **2009**, *131*, 985–992.

52. Profeta, M.; Mauri, F.; Pickard, C. J. *J. Am. Chem. Soc.* **2003**, *125*, 541–548.

53. Widdifield, C. M.; Bryce, D. L. *Phys. Chem. Chem. Phys.* **2009**, *11*, 7120–7122.

54. Perras, F. A.; Bryce, D. L. *J. Phys. Chem. C* **2012**, *116*, 19472–19482.

55. Perras, F. A.; Korobkov, I.; Bryce, D. L. *CrystEngComm* **2013**, *15*, 8727–8738.

56. Hampson, M. R.; Hodgkinson, P.; Evans, J. S. O.; Harris, R. K.; King, I. J.; Allen, S.; Fayon, F. *Chem. Commun.* **2004**, 392–393.

57. Hampson, M. R.; Evans, J. O.; Hodgkinson, P. *J. Am. Chem. Soc.* **2005**, *127*, 15175–15181.

58. Hibble, S. J.; Chippindale, A. M.; Marelli, E.; Kroeker, S.; Michaelis, V. K.; Greer, B. J.; Aguiar, P. M.; Bilbé, E. J.; Barney, E. R.; Hannon, A. C. *J. Am. Chem. Soc.* **2013**, *135*, 16478–16489.

59. Werner-Zwanziger, U.; Chapman, K. W.; Zwanziger, J. W. *Zeit. Phys. Chem*. **2012**, *226*, 1205–1218.

60. Epifani, M.; Imperatori, P.; Mirenghi, L.; Schioppa, M; Siciliano, P. *Chem. Mater.* **2004**, *16*, 5495–5501.

61. Millner, T.; Neugebauer, J. *Nature* **1949**, *163*, 601–602.

62. Rodriguez-Carvajal, J. Full Prof.2k, Vers. 5.30; 2012. http://www.ill.eu/sites/fullprof/.

63. Johnson, M. B.; White, M. A. Thermal Methods. In *Inorganic Materials: Multi Length-Scale Characterisation*; Bruce, D. W.; OHare, D.; Walton, R. I., Eds.; Wiley: New York, 2014; p 63–119.

64. Kentgens, A. P. M.; Verhagen, R. *Chem. Phys. Lett.* **1999**, *300*, 435–443.

65. Perras, F. A.; Viger-Gravel, J.; Burgess, K. M. N.; Bryce, D. L. *Solid State Nucl. Magn. Reson.* **2013**, *51–52*, 1–15.

66. Frydman, L.; Harwood, J. S. *J. Am. Chem. Soc.* **1995**, *117*, 5367–5368.

67. Amoureux, J.-P.; Fernandez, C.; Steuernagel, S. *J. Magn. Reson., Ser. A* **1996**, *123*, 116–118.
68. Millot, Y.; Man, P. P. *Solid State NMR* **2002**, *21*, 21–43.
69. Perras, F. A.; Widdifield, C. M.; Bryce, D. L. *Solid State Nucl. Magn. Reson.* **2012**, *45–46*, 36–34.
70. Massiot, D.; Fayon, F.; Capron, M.; King, I.; Le Calvé, S.; Alonso, B.; Durand, J.-O.; Bujoli, B.; Gan, Z.; Hoatson, G. *Magn. Reson. Chem.* **2002**, *40*, 70–76.
71. Massiot, D.; Hiet, J.; Pellerin, N.; Fayon, F.; Deschamps, M.; Steuernagel, S.; Grandinetti, P. J. *J. Magn. Reson.* **2006**, *181*, 310–315.
72. Clark, S. J.; Segall, M. D.; Pickard, C. J.; Hasnip, P. J,; Probert, M. I. J.; Refson, K.; Payne, M. C. *Z. Kristallogr.* **2005**, *220*, 567–570.
73. Charpentier, T.; Solid State Nucl. Magn. Reson. **2011**, *40*, 1–20.
74. Bonhomme, C.; Gervais, C.; Babonneau, F.; Coelho, C.; Pourpoint, F.; Azaïs, T.; Ashbrook, S. E.; Griffin, J. M.; Yates, J. R.; Mauri, F.; Pickard, C. J. *Chem. Rev.* **2012**, *112*, 5733–5779.
75. Perdew, J. P.; Burke, K.; Ernzerhof, M. *Phys. Rev. Lett.* **1996**, *77*, 3865–3868.
76. te Velde, G.; Bickelhaupt, F. M.; Baerends, E. J.; Fonseca Guerra, C.; van Gisbergen, S. J. A.; Snijders, J. G.; Ziegler, T. *J. Comput. Chem.* **2001**, *22*, 931–967.
77. van Lenthe, E.; Baerends, E. J.; Snijders, J. G. *J. Chem. Phys.* **1993**, *99*, 4597–4610.
78. Asmani, M.; Kermel, C.; Leriche, A.; Ourak, M. *J. Eur. Ceram. Soc.* **2001**, *21*, 1081–1086.
79. Romao, C. P.; Miller, K. J.; Johnson, M. B.; Zwanziger, J. W.; Marinkovic, B. A.; White, M. A. *Phys. Rev. B* **2014**, *90*, 024305-1–024305-9.
80. Soares, A. R.; Pontón, P. I.; Mancic, L.; d'Almeida, J. R. M.; Romao, C. P.; White, M. A.; Marinkovic, B. A. *J. Mater. Sci*. **2014**, *49*, 7870–7882.
81. Miller, K. J.; Johnson, M. B.; White, M. A.; Marinkovic, B. A. *Solid State Commun.* **2012**, *152*, 1748–1752.
82. Kingery, W. D., *J. Am. Ceram. Soc.* **1955**, *38*, 3–15.
83. Carter, B.; Norton, M.G., *Ceramic Materials Science and Engineering*; Springer, New York, New York, 2007.
84. Roy, R.; Agrawal, D. K; McKinstry, H. A., *Ann. Rev. Mater. Sci*. **1989**, *19*, 59–81.
85. Favre-Nicolin, V.; Černý, R. *J. Appl. Cryst.* **2002**, *35*, 734–743.

86. Pallister, P. J.; Moudrakovski, I. L.; Ripmeester, J. A. *Phys. Chem. Chem. Phys.* **2009**, *11*, 11487–11500.

87. Pauvert, O.; Fayon, F.; Rakhmatullin, A.; Krämer, S.; Horvatić, M.; Avignant, D.; Berthier, C.; Deschamps, M.; Massiot, D.; Bessada, C. *Inorg. Chem.* **2009**, *48*, 8709–8717.

88. Forgeron, M. A. M.; Wasylishen, R. E. *Phys. Chem. Chem. Phys.* **2008**, *10*, 574–581.

89. Ghose, S.; Tsang, T. *Am. Mineral.* **1973**, *58*, 748–755.

90. Burgess, K. M. N.; Xu, Y.; Leclerc, M. C.; Bryce, D. L. *J. Phys. Chem A* **2013**, *117*, 6561–6570.

91. Brändén, C.-I.; Jones, T. A. *Nature* **1990**, *343*, 687–689.

92. Brünger, A. T. *Nature* **1992**, *355*, 472–475.

93. Cornilescu, G.; Marquardt, J. L.; Ottiger, M.; Bax, A. *J. Am. Chem. Soc.* **1998**, *120*, 6836–6837.

94. Turner, G. L.; Chung, S. E.; Oldfield, E. *J. Magn. Reson.* **1985**, *64*, 316–324.

95. Engelhardt, G.; Kentgens, A. P. M.; Koller, H.; Samoson, A. *Solid State Nucl. Magn. Reson.* **1999**, *15*, 171–180.

96. Amoureux, J.-P.; Huguenard, C.; Engelke, F.; Taulelle, F. *Chem. Phys. Lett.* **2002**, *356*, 497–504.

97. Kaupp, M.; Malkina, O. L.; Malkin, V. G.; Pyykkö, P. *Chem. Eur. J.* **1998**, *4*, 118–126.

98. Yamamura, Y.; Ikeuchi, S.; Saito, K. *Chem. Mater.* **2009**, *21*, 3008–3016.

99. Torres Dias, A. C.; Luz Lima, C.; Paraguassu, W.; Pereira da Silva, K.; Freire, P. T. C.; Mendes Filho, J.; Marinkovic, B.; Miller, K. J.; White, M. A.; Souza Filho, A. G. *Vib. Spectrosc.* **2013**, *68*, 251–256.

100. Maczka, M.; Paraguassu, W.; Souza Filho, A. G.; Freire, P. T. C.; Mendes Filho, J.; Melo, F. E. A.; Hanuza, J. *J. Solid State Chem.* **2004**, *177*, 2002–2006.

101. M. W. Barsoum, *Fundamentals of Ceramics*; CRC Press, Boca Raton, Florida, 2002.

102. Imanaka, N.; Kobyashi, Y.; Tamura, S.; Adachi, G. *Solid State Ionics* **2000**, *136–137*, 319–324.

103. Harrison, W. T. A. *Mater. Res. Bull.* **1995**, *30*, 1325–1331.

104. Ari, M.; Jardim, P. M.; Marinkovic, B. A.; Rizzo, F.; Ferreira, F. F. *J. Solid State Chem.* **2008**, *181*, 1472– 1479.

105. Woodcock, D. A.; Lightfoot, P.; Ritter, C. *J. Solid State Chem.* **2000**, *149*, 92–98.

106. Imanaka, N.; Hiraiwa, M.; Adachi, G.; Dabkowska, H.; Dabkowski, A. 2000 *J. Cryst. Growth* **2000**, *149*, 176–179.

107. Balamurugan, S.; Rodewald, U. C.; Harmening, T.; van Wuellen, L.; Mohr, D.; Eckert, H.; Poettgen, R. *Z. Naturforsch., B: Chem. Sci.* **2010**, *65*, 13–17.

108. Evans, J. S. O.; Mary, T. A. *Int. J. Inorg. Mater.* **2000**, *2*, 143–151.

109. Guzmán-Afonso, C.; González-Silgo, C.; González-Platas, J.; Torres, M. E.; Lozano-Gorrín, A. D.; Sabalisck, N.; Sánchez-Fajardo, V.; Campo, J.; Rodríguez-Carvajal, J. *J. Phys.: Condens. Matter* **2011**, *23*, 325402:1–325402:9.

110. Sumithra, S.; Umarji, A. M. *Solid State Sci.* **2006**, *8*, 1453–1458.

111. Makovicky, E.; Balic-Žunić, T. *J. Appl. Cryst.* **1996**, *29*, 305–306.

112. Shannon, R. D. *Acta. Cryst. A* **1976**, *32*, 751–767.

113. Sumithra, S.; Umarji, A. M. *Solid State Sci.* **2004**, *6*, 1313–1319.

114. Nassau, K.; Levinstein, H. J.; Loiacono, G. M. *J. Phys. Chem. Solids.* **1965**, *26*, 1805–1816.

115. Dietzel, A. *Z. Elektrochem.* **1948**, *48*, 9–23.

116. Altermatt, D.; Brown, I. D. *Acta Cryst. B* **1985**, *41*, 244–247.

117. Varga, T.; Wilkinson, A. P.; Lind, C.; Bassett, W. A.; Zha, C.-S. *J. Phys.: Condens. Matter* **2005**, *17*, 4271–4283.

118. Varga, T.; Wilkinson, A. P.; Lind, C.; Bassett, W. A.; Zha, C.-S. *Phys. Rev. B* **2005**, *71*, 214106-1–214106-8.

119. Karmakar, S.; Deb, S. K.; Tyagi, A. K.; Sharma, S. M. *J. Solid State Chem* **2004**, *177*, 4087–4092.